Journal of Materials Chemistry A

ROYAL SOCIETY OF CHEMISTRY

REVIEW

View Article Online
View Journal | View Issue



Cite this: J. Mater. Chem. A, 2022, 10, 19184

# Reactive oxygen species on transition metal-based catalysts for sustainable environmental applications

Yonglin Wen,†[ab] Jiawei Yan,†[ab] Bixia Yang,[ab] Zanyong Zhuang *[ab] and Yan Yu*[ab]

Received 20th March 2022
Accepted 18th May 2022

DOI: 10.1039/d2ta02188a

rsc.li/materials-a

Tailoring reactive oxygen species (ROS) in advanced oxidation processes (AOPs) in a controlled manner is essential in chemical synthesis and environmental applications. In this paper, we begin with an overview of four ROS, and summarize methods and various precursors (*e.g.*, $O_2$, $H_2O_2$, and persulfate) to generate particular ROS. We then examine the use of the ROS in the degradation of pollutants and in the synthesis of value-added chemicals. We highlight the use and mechanism response of transition metal catalysts, generally developed with defect engineering, in advancing AOPs. We conclude with an outlook of current challenges and future perspectives of applying ROS in AOPs. We anticipate this review to inspire researchers to develop green, safe, and efficient ROS systems for sustainable environmental applications.



## 1 Introduction

The growing consumption of petrochemical products is quickly depleting petroleum and fossil resources worldwide and discharging organic pollutants into the environment. Efficient green techniques are needed to reduce pollution and to produce value-added chemicals from renewable feedstock.[1–4] Advanced oxidation processes (AOPs) mediated by reactive oxygen species (ROS) have been demonstrated in the past few decades as the underpinning of many essential applications in environmental protection and sustainable development.[5,6]

A key issue in developing suitable AOPs is finding the desired ROS with appropriate reactivity and selectivity.[7] Fenton chemistry has been used extensively since 1894 to create the hydroxyl radical ($HO^{\bullet}$), a powerful radical that can degrade toxic organic substrates thoroughly to $CO_2$ and $H_2O$. However, $HO^{\bullet}$ has a short half-life and cannot be sustained in multi-step processes, and continuous addition of its precursor (*e.g.* $H_2O_2$) is required to produce a sufficient amount of $HO^{\bullet}$ to ensure effective degradation of pollutants.[8] Moreover, although it has long been used for the thorough degradation of recalcitrant organic contaminants to $CO_2$ and $H_2O$, it has limited applications in chemical synthesis or biomass conversion, as its high reactivity may cause undesired over-oxidation and degradation.[9] Alternatively, researchers found that the superoxide radical ($O_2^{\bullet-}$) and singlet oxygen ($^1O_2$) can also engage in AOPs, both of which have a longer half-life than $HO^{\bullet}$ as well as a more moderate oxidation potential suitable for controlled oxidation.

[a]College of Materials Science and Engineering, Fuzhou University, New Campus, Minhou, Fujian 350108, China. E-mail: zyzhuang@fzu.edu.cn; yuyan@fzu.edu.cn
[b]Key Laboratory of Advanced Materials Technologies, Fuzhou University, Fuzhou 350108, China
† Y. Wen and J. Yan contributed equally to this work.

*Yonglin Wen received his BSc in materials science and engineering from Fuzhou University. He is currently pursuing his PhD degree at Fuzhou University under the supervision of Prof. Yu and Prof. Zhuang. His research focuses on the design of Mn-based catalysts for heterogeneous oxidation catalysis and biomass conversion.*

*Jiawei Yan received his BSc in materials science and engineering from Fujian Agriculture and Forestry University. He is currently pursuing his PhD degree at Fuzhou University under the supervision of Prof. Zhuang and Prof. Yu. His research focuses on the design of transition metal-based materials deployed for advanced oxidation processes.*

In addition to these ROS generated over the catalysts, the lattice oxygen ($O_L$) of transition metal oxides (TMO) can serve as a moderate ROS in heterogeneous AOPs to directly oxidize organic matter, and it has allowed successful oxidation reactions based on thermocatalysis, photocatalysis, electrocatalysis, *etc.*[10,11] Using $O_L$ in chemical synthesis and biomass conversion is advantageous in that it can selectively oxidize the organic substrate and avoid over-oxidation.

Heterogeneous transition metal-based catalysts (*e.g.*, oxides,[12] hydroxides,[13,14] oxyhydroxides,[15] and sulfides[16]) are readily used in AOPs. Their advantages include earth abundance, high stability, low cost, *etc.*[17] AOPs using heterogeneous catalysts manipulate the geometrical and/or electronic states of the precursors (*e.g.*, $H_2O_2$, $O_2$, PMS, PDS, and TMO) to create ROS on the catalyst surfaces. Hence, surface and defect engineering has emerged in recent years as a popular and appealing technique to customize the catalyst and more effectively activate the percursors.[18–21] There are substantial developments in the rational design of deficient transition metal-based materials deployed for advancing AOP strategies.[22–26] Anionic vacancies (*e.g.*, oxygen, sulfur, and nitrogen) introduced to transition metal-based catalysts as point defects always have a pronounced effect on the physical and chemical properties of the catalyst.[27,28] Engineering point defects creates new opportunities to afford advanced catalysts that can efficiently and selectively create ROS ($HO^{\bullet}$, $O_2^{\bullet-}$, $^1O_2$, $O_L$) from the precursors to thus carry out the AOP as intended.[29]

Understanding the reactivity and the selective generation of distinct ROS and identifying the mechanism response of deficient catalysts in AOPs are essential for the rational design of potent catalysts with fine-tuned oxidation behavior.[30] In this review, we firstly summarize the types and redox properties of ROS. We then systematically discuss the generation of ROS based on the precursor used and the methods to detect and identify the ROS. We also discuss defect engineering techniques that modify the catalyst surface and enable thorough or selective oxidation of organic matter. We next examine oxidation reactions that can be accomplished with the ROS. We finish with a brief comment on the current challenges and future developments of ROS in the burgeoning research area of AOPs.

## 2 Types of reactive oxygen species

### 2.1 Hydroxyl radical ($HO^{\bullet}$)

The hydroxy radical is highly reactive and has demonstrated widespread use as a nonselective reagent in AOPs for wastewater treatment, as it can initiate complex chain oxidation reactions to convert organic matter to oxidized products or ultimately to $CO_2$ and $H_2O$. In acidic media, $HO^{\bullet}$ has an extraordinarily high redox potential (2.8 V *versus* the normal hydrogen electrode, NHE) which is only second to that of fluorine.[31] It can attack most organic pollutants with a high rate constant of $10^6$ to $10^9$ $M^{-1}$ $s^{-1}$, which is about $10^3$ to $10^9$ times faster than that of molecular $O_2$ (1–$10^3$ $M^{-1}$ $s^{-1}$).[32] However, the reactivity of $HO^{\bullet}$ is pH-dependent according to the Nernst equation,[33] and its standard electrode potential drops to 1.55 V *vs.* NHE in basic media.[34] The $HO^{\bullet}$ in aqueous solution has a half-life ranging from picoseconds to nanoseconds, and its self-diffusion coefficient in water is estimated to be $2.8 \times 10^{-5}$ $cm^2$ $s^{-1}$. Hence, the diffusion distance of $HO^{\bullet}$ is a few molecular diameters away from where the $HO^{\bullet}$ is produced.[35,36]

Mechanistically, the oxidation of organic matter by $HO^{\bullet}$ may involve radical adduct formation, hydrogen abstraction, and electron transfer,[37] and is highly dependent on the types of functional groups in the organic substrate.[38] Because of its electrophilic nature, $HO^{\bullet}$ normally prefers to react with electron-rich sites such as C=C and C=N bonds in the organic substrate rather than the C=O bonds whose carbon atom is electron-deficient.[39] The C–H bonds of saturated aliphatic compounds that have relatively small dissociation energy can experience hydrogen abstraction.[40]

### 2.2 Superoxide radical ($O_2^{\bullet-}$)

The superoxide radical, first proposed in 1934 as the radical anion in the potassium salt,[41] is a relatively small univalent anion with an O–O bond distance between that of $O_2$ and peroxide.[42] The ground-state triplet molecular oxygen ($O_2$) has

*Zanyong Zhuang received his BS degree (2006) in chemistry from Xiamen University, and PhD degree (2011) from the Fujian Institute of Research on the Structure of Matter (FJIRSM), Chinese Academy of Sciences (CAS). Currently, he is a full professor at Fuzhou University. His research interests mainly focus on the rational design of transition metal-based catalysts for energy and environmental applications, including advanced oxidation reactions and $CO_2$ reduction reactions.*

*Yan Yu received her BS, MS, and PhD degrees from Fuzhou University. She was a post-doctoral fellow from 2010–2013 at the Fujian Institue of Research on the Structure of Matter (FJIRSM), Chinese Academy of Sciences (CAS). Currently, she is a full professor at Fuzhou University. Her research interests include environmental remediation, water purification, ecological materials, and photocatalytic $CO_2$ reduction, and $H_2$ production.*

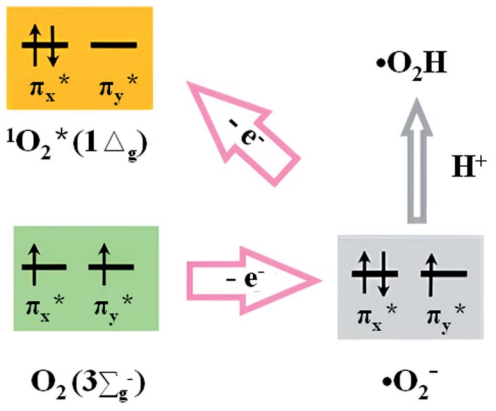


Fig. 1 Molecular π* orbitals for $O_2$, $^1O_2$, and $O_2^{\bullet-}$.[33]

two electrons occupying the separated π* orbitals of parallel spins (Fig. 1). When the ground-state $O_2$ participates in the redox reaction, the reductants need to offer a pair of electrons of the same spin states, so that the electrons from reductants can fit into the vacant spaces in the π* orbitals of oxygen.[33] Due to this limitation, the ground-state $O_2$ is normally of weak oxidizing capacity *via* the 2-electron transfer process. $O_2^{\bullet-}$ can be formed by one-electron reduction of $O_2$, or by filling the two π* orbitals of $O_2$ with an electron followed by protonation (Fig. 1). The homonuclear diatomic radical $O_2^{\bullet-}$ has a slightly lower redox potential (2.4 V *vs.* RHE) than HO•,[43] and has demonstrated critical roles in chemical, biological, and environmental applications. Note that (somewhat perplexingly) $O_2^{\bullet-}$ also has a reducing potential of $E_0$ ($O_2/O_2^{\bullet-}$) = −0.33 V and can be oxidized by a ferricenium ion to give singlet oxygen ($^1O_2$),[44] because it has an extra electron in one of its π* antibonding orbitals compared to ground state dioxygen ($^3O_2$). The redox potential of $E_0$ ($O_2/O_2^{\bullet-}$) does no change with pH when the pH value is >4.8. At pH value <4.8, $O_2^{\bullet-}$ will be protonated at pH < 4.8 which creates the perhydroxyl radical ($^{\bullet}O_2H$) of reduction potential $E_0$ ($O_2$, $H^+/^{\bullet}O_2H$) = −0.046 V *vs.* NHE.[31,33] The half-life of $O_2^{\bullet-}$ can reach up to 51–422 s at pH = 2–10,[45] much longer than those of HO• and $^1O_2$.[46] It means $O_2^{\bullet-}$ can be prepared and work under alkaline conditions. The diffusion distance of $O_2^{\bullet-}$ has been estimated to be about 35 μm, assuming a general diffusion coefficient (about 105 $cm^2$ $s^{-1}$) of small molecules.[47]

However HO• is electrophilic, and $O_2^{\bullet-}$ can be both nucleophilic and electrophilic. The half-life of $O_2^{\bullet-}$ is up to 51–422 s at pH = 2–10,[45] which is longer than that of HO• and $^1O_2$.[46] Hence, $O_2^{\bullet-}$ can be prepared and stabilized in strongly basic aqueous solutions. It is readily used to scavenge organic pollutants, such as treating pollutants in underground water under anoxic conditions,[33,48,49] and can serve as a major ROS for the degradation of organic compounds such as bisphenol A (BPA) and dyes.[50,51] However, HO• is highly active, and nonselective and tends to react with organic solvents; $O_2^{\bullet-}$ can be used for the partial or selective oxidation of substrates in organic solvents.[33,52–54]

The reaction of organic matter with $O_2^{\bullet-}$ may involve radical adduct formation, hydrogen abstraction, and electron transfer. Transferable hydrogen atoms on the substrates can be readily removed by $O_2^{\bullet-}$ (*e.g.*, dihydrophenazine to phenazine radical, *N*-methylhydrophenazine to *N*-methylphenazine radical).[55] When $O_2^{\bullet-}$ reacts with organic compounds *via* hydrogen abstraction, it generates carbon-based radicals that can further combine with oxygen to form peroxy intermediates that will decompose further. The nucleophilic substitution reaction of $O_2^{\bullet-}$ was first reported in 1970,[56,57] and $O_2^{\bullet-}$ can react with alkyl halides *via* nucleophilic substitution to break the C–Cl bond to give dechlorinated products.[58] Besides, $O_2^{\bullet-}$ is found to also react with α-keto, α-hydroxy, and α-halo carbonyl compounds *via* nucleophilic addition at the carbonyl carbon, and the ensuing oxidative cleavage gives carboxylic acids.[59] As a nucleophile, $O_2^{\bullet-}$ can attack the carbonyl carbon of esters to yield carboxylic acid anions and alcohols, and the carbonyl carbon of acyl halides to yield diacyl peroxides.[42] Interestingly, $O_2^{\bullet-}$ may also act as a reducing agent in one-electron transfer reductions, and reactions involving electron transfer from $O_2^{\bullet-}$ to organic substrates (*e.g.*, nitroblue tetrazolium) have been exploited to detect or quantify $O_2^{\bullet-}$.[33]

### 2.3 Singlet oxygen ($^1O_2$)

There have been reports on using $^1O_2$ in the synthesis of chemicals and natural products since the 1980s.[60] Energy transfer to $O_2$ could create singlet oxygen ($^1O_2$). $^1O_2$ has paired electrons of opposite spins (Fig. 1), manifesting higher reactivity compared with the ground-state $O_2$. As the unstable, excited state of molecular oxygen, $^1O_2$ has a lower redox potential (0.81 V *vs.* NHE) than $O_2^{\bullet-}$ and HO•. The paired electrons in the external orbital of $^1O_2$ have antiparallel spins.[61] The reaction rate of $^1O_2$ with organic compounds generally ranges in $10^4$ to $10^7$ $M^{-1}$ $s^{-1}$. The half-life of $^1O_2$ ($^1\Delta_g$ state) is several tens of milliseconds in air but only as short as 3 μs in water.[33] A growing body of work has suggested that the redox potential of $^1O_2$ does not change significantly with the pH value, so that the $^1O_2$ can work in a wide pH range and exhibit considerable tolerance to environmental interference. Note that the half-life of $^1O_2$ ($^1\Delta_g$ state) is several tens of milliseconds in air but only as short as 3 μs in water.[33] This very short half-life and the short diffusion distance (~220 nm) restrict the reactivity of $^1O_2$ to the proximity of where it is formed.[62] As a result, it is less effective to rapidly remove organic pollutants in an aqueous environment by $^1O_2$.[58,63]

Nevertheless, $^1O_2$ can be exploited as a moderate oxidant for selective or partial oxidations in chemical synthesis,[43] such as the selective oxidation of various organic substrates including amines, alcohols, olefins, and sulfides.[31,64–66] Studies have shown that $^1O_2$ can oxidize unsaturated organic compounds by electrophilic attack and electron abstraction. For instance, the electrophilic attack of $^1O_2$ to dioxin and furan gives endoperoxide intermediates,[67] and the photosensitized oxygenation of phenol proceeds *via* hydrogen abstraction by $^1O_2$.[68] Because $^1O_2$ is an excited state of $O_2$, it may be deactivated to the original stable $^3O_2$ without undergoing chemical reactions or electron transfer.

### 2.4 Surface lattice oxygen ($O^{2-x}$)

The lattice oxygen ($O_L$) of transition metal oxides (TMO) can directly oxidize organic matter through the Mars–van Krevelen

 

(MvK) redox cycle.[69,70] In the MvK mechanism, the substrate is firstly oxidized by the $O_L$ in the oxides, leaving behind an oxygen vacancy (OV) on the TMO surface that will be subsequently oxidized by $O_2$, *i.e.*, the stoichiometric oxidant, to regenerate $O_L$. The reactivity of $O_L$ depends strongly on the formation of OVs from the oxides, the local coordination environment of the $O_L$ in oxides, and the strength of the M–O bond, and is sensitive to defects (or impurities), the composition, the surface, the interface, *etc.*[71,72] Normally TMO with transition metals of high valence state exhibit superior $O_L$ activity. However reactions based on $HO^{\bullet}$, $O_2^{\bullet-}$, and $^1O_2$ normally proceed at room temperature and the reactivity weakens at elevated temperatures;[73,74] $O_L$ can serve as an appealing oxidation reagent at elevated temperatures.

Because $O_L$ is nucleophilic and has a lower redox potential, the oxidation of hydrocarbons with $O_L$ can give products in which all C–C bonds are retained (partial oxidation), which is in clear contrast to the electrophilic oxidation (*e.g.*, by $HO^{\bullet}$) that cleaves all C–C bonds.[75] Thus, $O_L$ is readily used for the selective oxidation of biomass for sustainable development, as it can avoid undesired oxidative degradation. The use of $O_L$ is also key in soot combustion, the oxidation of CO and $NO_x$, and the thermal oxidation of pollutants such as volatile organic compounds (VOC).[76–78]

## 3 Generation of reactive oxygen species

Manipulating the geometrical and electron states of various precursors ($H_2O_2$, $O_2$, persulfates, and TMO) is key to generating ROS. In recent years, engineering point defects (*e.g.*, anionic vacancies) on crystals (*e.g.*, TMO) has emerged as an effective strategy to create catalytically active surfaces that help generate ROS. The deficient structure can strongly adsorb and activate the precursor oxidants (*e.g.*, $H_2O_2$, $O_2$, PMS, and PDS) by elongating the chemical bond (*e.g.*, the O–O bond in $H_2O_2$).[79] The electrons conducted from the bulk to the surface of the crystal may be trapped in the vacancies to create electron-rich regions[80] as additional carriers for surface reactions to generate ROS.[81] For catalytic reactions using $O_L$ in oxides as the ROS, the defect structure of oxides can help create $O_L$ of high reactivity by increasing the $O_L$ mobility and/or by promoting $O_L$ regeneration.

(1) Activation of $H_2O_2$: hydrogen peroxide ($H_2O_2$) is a unique, versatile, green oxidizing agent for AOPs, as it has a high active oxygen content and gives $H_2O$ as the only reduction product. However, due to its low redox potential (1.77 eV), it does not readily oxidize organic compounds on its own,[82] and Fenton chemistry is exploited to activate the $H_2O_2$ to generate ROS. The classic, well-known homogeneous Fenton reaction system based on $Fe^{2+}/H_2O_2$ suffers from several drawbacks that impede large-scale applications, such as a narrow working pH range (mostly acidic), generation of iron-containing sludge, and limited activity.[83] These hurdles prompted efforts to investigate the heterogeneous activation of $H_2O_2$ with transition metal-based catalysts, with which the type and amount of ROS can be regulated through distinct surface reactions. Although the decomposition of $H_2O_2$ on the catalyst surface is always spontaneous in 25–286 °C,[84] the activation energy (20.93–96.30 kJ $mol^{-1}$) and the rate of ROS generation depend heavily on the surface structure of the catalysts.[85,86]

(2) Activation of persulfates: peroxymonosulfate (PMS and $HSO_5^-$) and peroxydisulfate (PDS and $S_2O_8^{2-}$) are relatively strong oxidizers with redox potentials of 1.82 and 2.01 V, respectively. AOPs with persulfates were introduced for groundwater remediation in the late 1990s, because methods to activate persulfates are more abundant and the availability of persulfate salts reduces storage and transportation costs.[87] Additionally, PMS and PDS attain a higher radical yield, and the treatment efficiency is less dependent on the operational parameters (*e.g.*, pH, initial peroxide loading, and background constituents). Moreover, the activation of PMS/PDS on transition metal-based catalysts is usually carried out under alkali conditions.[88] Hence, persulfate AOPs are good substitutes of Fenton chemistry with $H_2O_2$. The energy of the O–O bond in PMS is estimated to be in 140–213.3 kJ $mol^{-1}$, and the activation requires adequate energy input. Appropriate activation of PMS and PDS to give ROS is imperative to ensure the desired oxidation performance, since PMS and PDS react directly with the organic contaminants only at a low rate.[89] They can be activated with metal catalysts,[90] carbon nanotubes,[91] biochars,[92] TMO,[93] *etc.*

(3) Activation of $O_2$: among all oxidants, oxygen is the most environmentally friendly, inexpensive, and accessible.[94] Due to the spin-flip restriction, molecular $O_2$ is normally at the ground triplet state ($^3O_2$) and cannot directly engage in aerobic oxidation.[95] The activation of molecular $O_2$ into ROS ($HO^{\bullet}$, $O_2^{\bullet-}$, and $^1O_2$) is normally a fundamental step in aerobic catalytic oxidation reactions.[96,97] However, the O=O bond of $O_2$ has a high bond energy (498 kJ $mol^{-1}$) that must be overcome to initiate $O_2$-mediated oxidation reactions. Transition metal-based catalysts (*e.g.*, transition metal complexes,[98] TMO,[99] and transition metal sulfides[100]) critically improve the reactivity of $O_2$ by effectively adsorbing the $O_2$ molecules and weakening the O=O bond of $O_2$ through efficient charge transfer, and photocatalysis is frequently used to promote electron transfer in the activation of $O_2$.[101]

(4) Lattice oxygen: metal oxides are the carrier of $O_L$ and they maintain the lattice structure throughout the reaction. The MvK mechanism of $O_L$-mediating oxidation is well supported by isotope labelling, as using $^{18}O_2$ as the stoichiometric oxidant will install $^{18}O$ in the lattice of the metal oxides.[102] Heating is generally required to activate $O_L$ and regenerate $O_L$ from $O_2$, which can increase cost and make the reaction procedure tedious. The reactivity and regeneration of $O_L$ can be tuned by regulating the strength of the M–O bond (M: metal) and the chemical states of the metal, to enable stronger oxidation performance at a lower temperature.[103] Anionic vacancies on the metal oxides change the electronic state and the surface structure, and they can improve the adsorption of $O_2$, reduce the energy of the M–O bond, modify the electron density distribution, change the ion transport in the crystal, and expedite the

migration of $O_L$.[104] Doping metal oxides with heteroatoms is an appealing method to create such vacancies.

### 3.1 Hydroxyl radical

**3.1.1 From $H_2O_2$.** HO$^\bullet$ can be deemed a reduction product of $H_2O_2$. The main ROS in the Fenton reaction involving $H_2O_2$ is the HO$^\bullet$ radical generated in the Haber–Weiss cycle. A traditional homogeneous Fenton system requires a large input of $Fe^{2+}$ (18–410 mmol $L^{-1}$) and excess $H_2O_2$ (30–6000 mmol $L^{-1}$) in the redox process to produce enough HO$^\bullet$ for practical applications.[105] Moreover, it generates iron sludge, has limited activity, and requires a specific working pH range. In the search for heterogeneous Fenton systems as efficient alternatives, researchers developed transition metal-based catalysts,[106,107] clay-based catalysts,[13] and zeolite-based catalysts[108–111] to accomplish Fenton chemistry, and external energy sources such as UV/visible irradiation, electricity, and ultrasound have also been used to boost the generation of HO$^\bullet$.[112,113] The decomposition of $H_2O_2$ over transition metal-based catalysts to create ROS deserves special comments because these catalysts have high stability, low cost, earth abundance, and potentially high catalytic activity. The surface OVs of deficient TMO such as $TiO_{2-x}$ can activate $H_2O_2$ to give HO$^\bullet$.[114] Zhang *et al.* reported that while the oxygen deficient $TiO_{2-x}$ readily activates $H_2O_2$ to generate HO$^\bullet$ to degrade methyl orange and *p*-nitrophenol, no HO$^\bullet$ is detected in the pristine $TiO_2/H_2O_2$ system.[115] Theoretical studies have been run to unveil how defect structures boost the $H_2O_2$ activation. For example, Density Functional Theory (DFT) calculations show that the adsorption of $H_2O_2$ is stronger on the deficient $\alpha$-$Fe_2O_3$ (001) surface than on the pristine surface.[116] The energy barrier of activation and the O–O bond length at the transition state are 3.65 kJ $mol^{-1}$ and 1.60 Å for $H_2O_2$ adsorbed on the $\alpha$-$Fe_2O_3$ surface with OVs, but 44.89 kJ $mol^{-1}$ and 1.75 Å on the pristine $\alpha$-$Fe_2O_3$ surface. Analogously, introducing S vacancies (SVs) in $Fe_3S_4$ (FS-100) creates strong peroxidase-like activity not available from SV-poor $Fe_3S_4$ (FS-0), which can be attributed to the efficient adsorption of $H_2O_2$ and its subsequent decomposition to HO$^\bullet$ at the SVs of $Fe_3S_4$ (Fig. 2a).[117] The adsorption energy of $H_2O_2$ is −7.15 eV on the (011) surface of SVs-free $Fe_3S_4$ but −6.01 eV for SVs-rich $Fe_3S_4$ (Fig. 2b). The length of the O–O bond is 1.515–1.525 Å for $H_2O_2$ on SVs-free $Fe_3S_4$ but 3.151–4.491 Å for $H_2O_2$ on SVs-$Fe_3S_4$ (Fig. 2c). In the case of deficient $CeO_2$, the key factor to the efficient generation of HO$^\bullet$ from $H_2O_2$ is the electron density of Ce adjacent to the

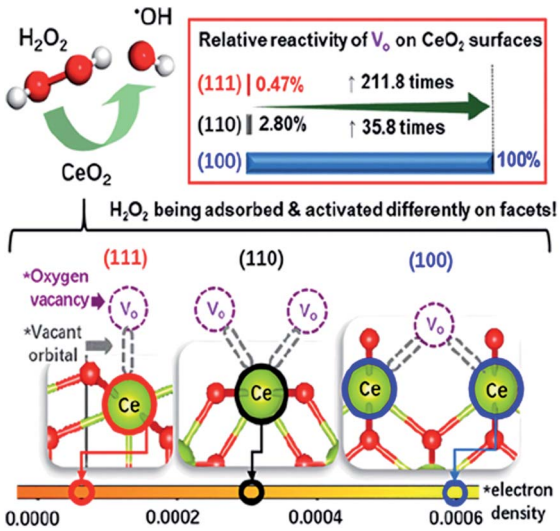


Fig. 3 Schematic illustration of the synergy effect of Ce and OVs on the $CeO_2$ surface for the efficient activation of $H_2O_2$ into HO$^\bullet$. Adapted with permission from ref. 118 Copyright (2020) American Chemical Society.

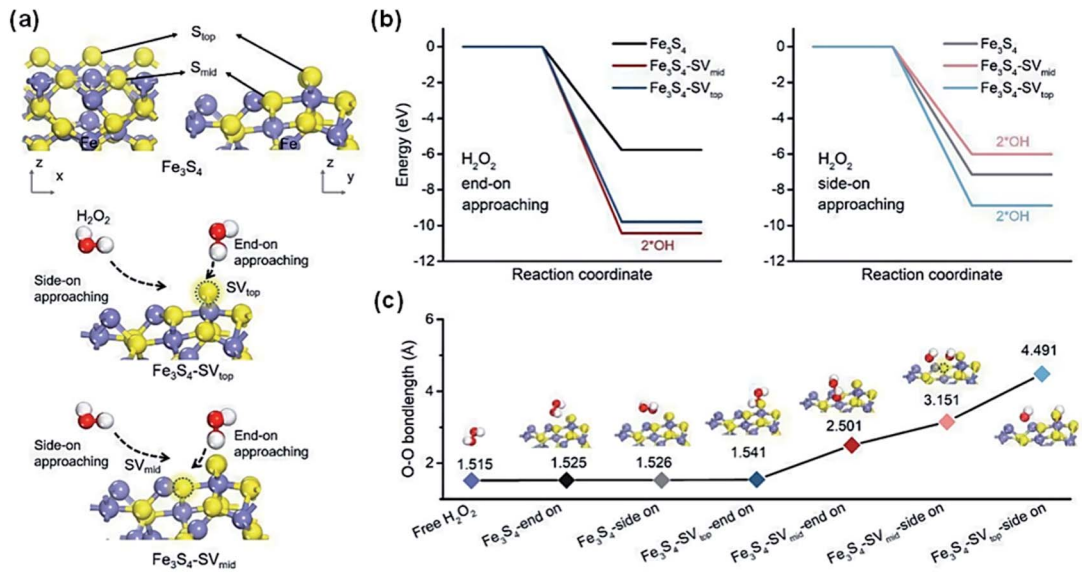


Fig. 2 (a) Models of $Fe_3S_4$ and SVs-rich $Fe_3S_4$ with exposure of the (011) surface. (b) Energy diagrams of $H_2O_2$ adsorption on SVs-rich $Fe_3S_4$ *via* end-on and side-on attachment models. (c) The O–O bond length of adsorbed $H_2O_2$ in different adsorption configurations. Adapted with permission from ref. 110 Copyright (2021) Elsevier.

 

OVs, and the strong adsorption of $H_2O_2$ at the metastable OVs on the (110) surface of $CeO_2$ alone does not guarantee the subsequent activation of $H_2O_2$ (Fig. 3).[118] Metastable OVs can be available for the catalytic cycle only when the electron density of the surface Ce is high enough to break the O–O bond of the adsorbed $H_2O_2$. In other words, a synergy exists between the geometry and the electronic state of the OVs to help adsorb and activate $H_2O_2$. The incorporation of Co into ZnO creates OV-rich Co–ZnO as a Fenton-like catalyst that features both electron-rich OVs with unpaired electrons and electron-deficient $Co^{3+}$ sites.[119] The electron-rich OVs help capture and reduce $H_2O_2$ to generate HO$^\bullet$ that can quickly degrade pollutants. The electron-deficient $Co^{3+}$ sites degrade the adsorbed organic pollutants through the electron transfer from the organics to $Co^{3+}$, which helps offset the imbalanced electron distribution in the doped oxide.

**3.1.2 From $O_2$.** Generating HO$^\bullet$ directly from $O_2$ has also been demonstrated. For example, low-valence Mn ions can act as an efficient Fenton-like reagent to reduce atmospheric $O_2$ to $H_2O_2$, which can subsequently generate HO$^\bullet$ (Fig. 4).[120] Catalyst surfaces with anionic vacancies can create HO$^\bullet$ from $O_2$ because of enhanced adsorption and electron migration. According to DFT calculations, less energy is required to break the O=O bond to generate HO$^\bullet$ when more electrons are transferred to $O_2$.[121] Setvin *et al.* used scanning tunnelling microscopy to pull the vacancies of an anatase crystal to its surface and proved that the surface OVs of $TiO_2$ can serve as electron donation sites to activate the adsorbed $O_2$.[122] In an example that is beyond the use of transition metals, Zhao *et al.* reported that the $O_2$ adsorbed on the surface of Pt SA/MgO with OVs can dissociate more easily to generate HO$^\bullet$.[123] The presence of OVs notably decreases the adsorption energy of $O_2$ ($E_{ads} = -3.25$ eV), elongates the O=O bond (from 1.363 to 1.552 Å), and decreases the energy barrier of activating $O_2$ (down to 2.48 eV). The $O_2$ molecule adsorbed on the surface of Pt SA/MgO gives two adsorbed oxygen atoms [denoted as *O] after the O=O bond is broken, and a further reaction between *O and adsorbed $H_2O$ gives HO$^\bullet$ (*i.e.*, $O_2 \rightarrow 2{*}O$, $*O + H_2O \rightarrow 2HO^\bullet$).

**3.1.3 From PMS and PDS.** The cleavage of peroxide bonds in persulfates by one-electron reduction could create $SO_4^{\bullet-}$ based on eqn (1) and (2).[88] The $SO_4^{\bullet-}$ could react with $H_2O$ to generate HO$^\bullet$ *via* eqn (3),[124–126] and the reaction rate constant of $SO_4^{\bullet-}$ to give HO$^\bullet$ can be significantly accelerated under alkaline conditions (*e.g.*, at pH = 13.0) as described by eqn (4).[127]

$$M^{n+} + HSO_5^{\bullet-} \rightarrow M^{(n+1)+} + SO_4^{\bullet-} + OH^- \quad (1)$$

$$M^{n+} + S_2O_8^{2-} \rightarrow M^{(n+1)+} + SO_4^{\bullet-} + SO_4^{2-} \quad (2)$$

$$SO_4^{\bullet-} + H_2O \rightarrow HO^\bullet + SO_4^{2-} + H^+ \quad (3)$$

$$SO_4^{\bullet-} + OH^- \rightarrow HO^\bullet + SO_4^{2-} \quad (4)$$

### 3.2 Superoxide radical

**3.2.1 From $H_2O_2$.** The Fenton reaction that activates $H_2O_2$ may also create $O_2^{\bullet-}$.[61] Haber and Weiss proposed that in the Fenton reaction under neutral pH, the oxidation of $Fe^{2+}$ by $O_2$ and the decomposition of $H_2O_2$ can give $O_2^{\bullet-}$.[128] The generation of $O_2^{\bullet-}$ can also be detected when deficient catalysts are used.[129] Introducing OVs to TMO can favor interfacial electron transfer to the adsorbed $H_2O_2$,[130] and the O–O bond of $H_2O_2$ elongated by OVs is more easily cleaved under neutral and even alkaline conditions.[131] Wei *et al.* demonstrated enhanced oxidative behavior of a $TiO_2$–$H_2O_2$ system that can be attributed to the activation of $H_2O_2$ by $TiO_2$,[132] and noted that $O_2^{\bullet-}$ can be stably adsorbed on the $TiO_2$ surface but HO$^\bullet$ cannot (Fig. 5). Wu *et al.* generated $O_2^{\bullet-}$ and HO$^\bullet$ from $H_2O_2$ using the single electron-trapped oxygen vacancies of bulk $TiO_2$ without any light irradiation,[130] although the mechanism of $H_2O_2$ activation and the role of ROS in the enhanced oxidation ability are still debatable.

**3.2.2 From $O_2$.** Using $O_2$ or air as the precursor of $O_2^{\bullet-}$ is preferred over using $H_2O_2$ because it is more environmentally friendly and more economically beneficial.[133–135] Photocatalysis is generally exploited to create $O_2^{\bullet-}$ by injecting a photo-generated electron into $O_2$. Upon light irradiation, the photo-generated electrons and holes have the probability to recombine into excitons due to the strong Coulomb interaction. The defect structure prevalent in advanced catalysts can create

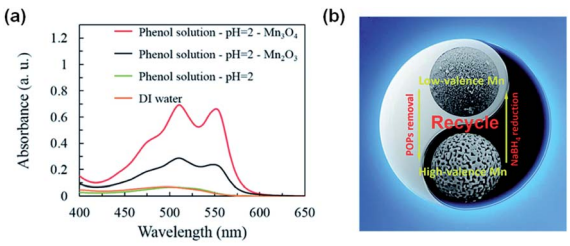


Fig. 4 (a) Detection of $H_2O_2$ by activation of $O_2$ over $Mn_3O_4$ and $Mn_2O_3$, respectively. (b) Schematic illustration of the recycling strategy for $Mn_3O_4$ and $Mn_2O_3$ on $O_2$ activation to generate $H_2O_2$ that decomposes into HO$^\bullet$. Adapted from ref. 120 with permission from The Royal Society of Chemistry.

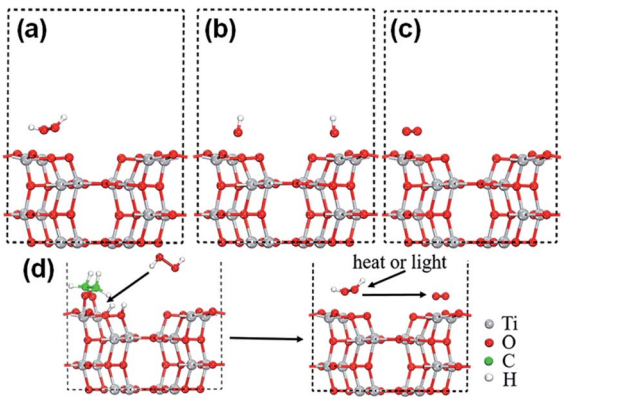


Fig. 5 Side view of (a) $H_2O_2$ (b) initial configuration of two hydroxyl groups, and (c) superoxide radicals adsorbed on the $TiO_2$ predicted by the GGA-TS method. (d) The decomposition mechanism of $H_2O_2$ into superoxide radicals on $TiO_2$ NSs. Adapted with permission from ref. 132 Copyright (2017) American Chemical Society.

defect levels in the band structure of catalysts, serving as the electron capturing center, to promote charge carrier separation and transfer to the catalytically active sites.[31] Therefore, photocatalysts with engineered defects with stronger electron migration can enhance $O_2$ activation in the catalytic reaction.[136] For example, the OVs of blue $TiO_2$ with localized electrons can facilitate the activation of $O_2$ to generate $O_2^{\bullet-}$ under visible-light irradiation.[137] OVs with localized electrons are the sites for the adsorption and activation of $O_2$, and the adsorption of $O_2$ on the perfect (101) surface of $TiO_2$ is much weaker. The adsorbed $O_2$ accumulates 1.1 e from the localized electrons of two unsaturated Ti atoms near the OVs of the $TiO_2$ surface and is activated into $O_2^{\bullet-}$ *via* a single-electron transfer pathway. In a similar manner, $O_2^{\bullet-}$ is generated from the reduction of dissolved $O_2$ in water with the electrons trapped in the vacancy sites on the surface of the highly reactive $CuFe_2O_4$ catalyst, and $O_2^{\bullet-}$ has stronger reactivity when it is on the solid surface than in the aqueous solution.[138] In another example, $Co_3O_4$ with OVs promotes the adsorption and reduction of $O_2$, and $O_2^{\bullet-}$ can be detected over the surface of $Co_3O_4$.[139] In the case of Ni–Fe layered double hydroxide (NiFe-LDH), OVs facilitate the charge carrier transfer of NiFe-LDH, and activate $O_2$ into $O_2^{\bullet-}$ for the selective oxidation of NO into nitrate (Fig. 6).[140] For the plasmonic catalyst of Au supported on OVs-BiOCl,[141] the OVs on BiOCl facilitate the trapping of plasmonic hot electrons, which are transferred to the adsorbed $O_2$ to give $O_2^{\bullet-}$ for the aerobic oxidation of benzyl alcohol. Although the presence of point defects could promote charge separation for enhanced ROS generation,[28] it must be noted that excessive OVs can be detrimental by trapping the electrons and restraining the electron mobility.[142] Besides the modulation of charge transfer, the introduction of point defects could create additional defect levels rendering either a downshift of the conduction band (CB) minimum of catalysts, or an upshift of the valence band (VB) maximum.[143,144] It has been reported that the OVs can lead to a down shift of the CB band of $BiO_{2-x}$, which benefits the electron transfer to $O_2$ molecules for the generation of $O_2^{\bullet-}$ efficiently.[145]

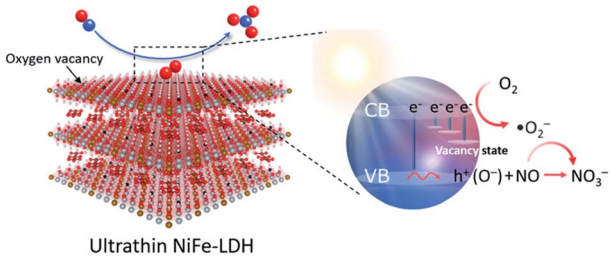


Fig. 6 Schematic illustration of activation of $O_2$ into $O_2^{\bullet-}$ on NiFe-LDH with an OV for the selective photocatalytic oxidation of NO. Adapted with permission from ref. 140 Copyright (2022) American Chemical Society.

In addition to OVs, S or N vacancies on the catalyst surface have also been exploited to tune the band structure and charge carrier transfer efficiency for $O_2$ activation on photocatalysts. For example, N vacancies can create electron-accumulated centers to activate $O_2$ over the Pt/$C_3N_4$ catalyst (Fig. 7b).[146] The length of the O=O bond is 1.496 Å for the activated $O_2$ over the N-doped catalyst but 1.260–1.365 Å in the control (Fig. 7a). The SVs on $In_2S_3$ nanosheets can activate $O_2$ into $O_2^{\bullet-}$ *via* enhanced electron transfer under visible light irradiation.[147] Theoretical calculations reveal that in the presence of the SVs, the density of states (DOS) of $In_2S_3$ is significantly enhanced at the valence band maximum (Fig. 7c and d). Consequently, electrons can be photoexcited to the conduction band and transferred to the

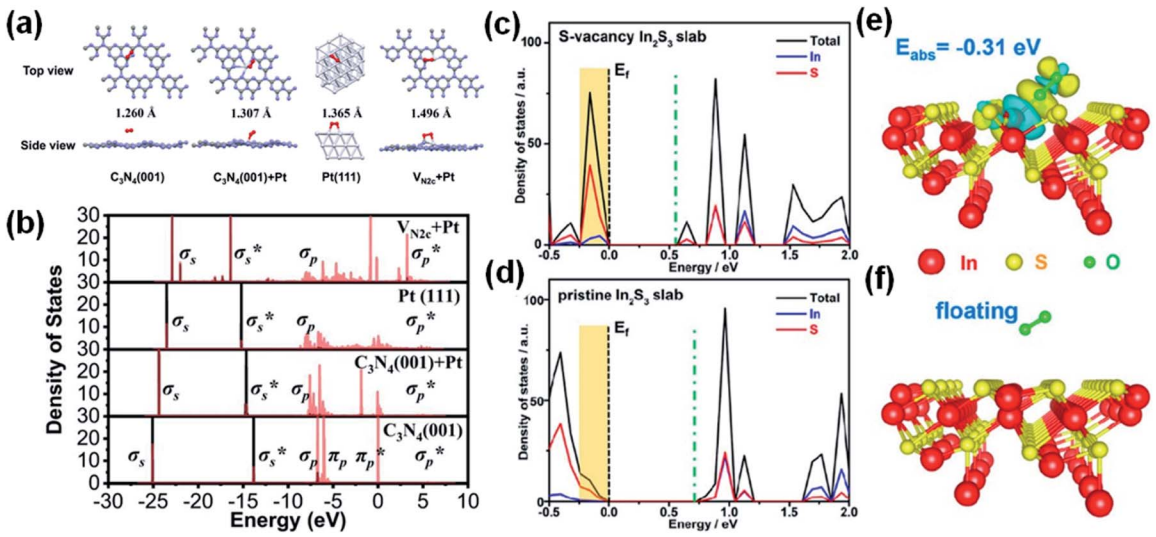


Fig. 7 (a) The structures of $O_2$ adsorbed on pure $C_3N_4$ (001), $C_3N_4$ (001) + Pt, Pt (111), and VN2c + Pt (gray, purple, white, and red represent C, N, Pt, and O). (b) Partial density of states (PDOS) of the adsorbed $O_2$ (black and red lines represent the O 2s and 2p orbitals, respectively). Adapted with permission from ref. 146 Copyright (2021) Springer Nature Group. Calculated DOS of (c) S-vacancy and (d) pristine $In_2S_3$ slabs ($E_f$ = Fermi level; orange shading indicates the increased DOS around the VBM). (e) The adsorption of $O_2$ at the S vacancy of the deficient $In_2S_3$ slab. (f) $O_2$ floating on the pristine $In_2S_3$ slab. Adapted with permission from ref. 147 Copyright (2022) American Chemical Society.

 

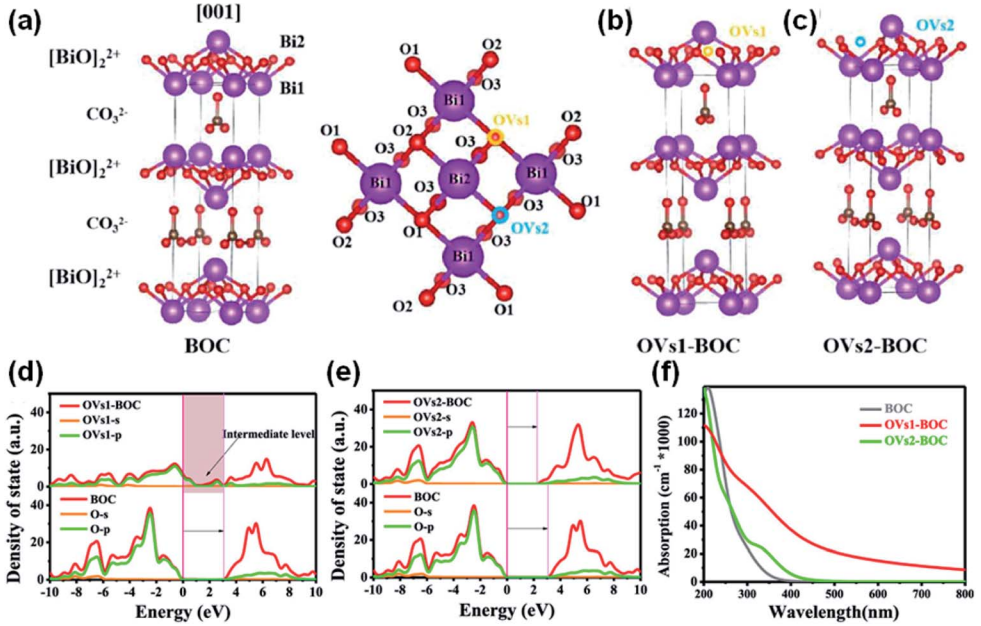


Fig. 8 The structural models of (a) BOC, (b) OVs1-BOC, and (c) OVs2-BOC, respectively. Contradistinction of DOS/PDOS (Fermi levels are set to 0 eV) between (d) BOC and OVs1-BOC and (e) BOC and OVs2-BOC. (f) Calculated optical absorption of BOC, OVs1-BOC, and OVs2-BOC. Adapted with permission from ref. 148 Copyright (2021) American Chemical Society.

defective surface more easily, and the defective $In_2S_3$ shows stronger interactions with $O_2$ than pristine $In_2S_3$ (Fig. 7e and f).

While the vacancies can directly inject localized electrons into $O_2$ to elongate the O=O bond and activate $O_2$, the geometry of the vacancies may tune the pathway of ROS generation by changing the band structure of catalysts. There are two different crystallographic positions of the oxygen atoms in the $[BiO]_2^{2+}$ layer of $(BiO)_2CO_3$ (referred to below as BOC), and Rao *et al.* constructed two kinds of OVs (*i.e.*, OVs1 and OVs2) in BOC by breaking Bi1-O1 or Bi2-O2 from two distinct lattice oxygens (O1 and O2) binding to the Bi atoms (Fig. 8a–c).[148] Both OVs1 and OVs2 extend the lifetime of photogenerated charge carriers in their respective photocatalytic systems and promote the efficient separation of carriers (Fig. 8d and e). While both OVs1 and OVs2 enhance light absorption in the visible region by introducing an intermediate level in the band gap, only OVs1 can enhance light absorption in the infrared region (Fig. 8f). The photogenerated charge carriers in OVs1 react with the adsorbed $O_2$ and $H_2O$ to form $O_2^{\bullet-}$ and $HO^{\bullet}$, respectively. In contrast, the observed redshift indicates that OVs2 decreases the optical bandgap energy of BOC, and $HO^{\bullet}$ cannot be generated on the catalyst surface with OVs2.

**3.2.3 From PMS and PDS.** PMS and PDS can be activated to generate $O_2^{\bullet-}$ as described in eqn (5)–(9). However, it has been suggested that $O_2^{\bullet-}$ frequently serves as an intermediate for the generation of other ROS (*e.g.*, $^1O_2$), rather than directly oxidizing the pollutant.[149]

$$HSO_5^- + H_2O \rightarrow HSO_4^- + H_2O_2 \quad (5)$$

$$SO_5^{2-} + H_2O \rightarrow SO_4^{2-} + H_2O_2 \quad (6)$$

$$H_2O_2 + HO^{\bullet} \rightarrow H_2O + H^+ + O_2^{\bullet-} \quad (7)$$

$$S_2O_8^{2-} + H_2O \rightarrow SO_5^{2-} + 2H^+ + SO_4^{2-} \quad (8)$$

$$S_2O_8^{2-} + HO_2^- \rightarrow SO_4^{\bullet-} + H^+ + O_2^{\bullet-} + SO_4^{2-} \quad (9)$$

### 3.3 Singlet oxygen

**3.3.1 From $H_2O_2$.** The decomposition pathway of $H_2O_2$ may also be regulated to give $^1O_2$.[150,151] While the superoxide radical ($O_2^{\bullet-}$) is produced from the catalytic activation of $H_2O_2$, in many cases it can undergo further disproportionation to produce $^1O_2$.[152] This pathway however cannot ensure the efficient and selective generation of $^1O_2$, as the Haber–Weiss reaction ($O_2^{\bullet-} + H_2O_2 \rightarrow HO^{\bullet} + OH^- + O_2$) significantly reduces

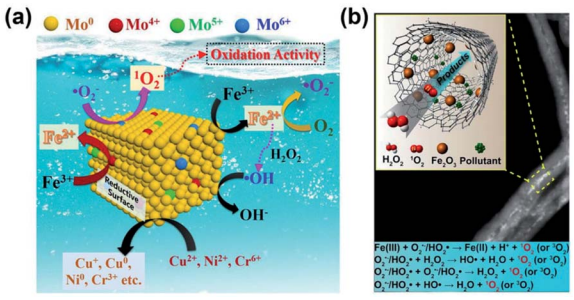


Fig. 9 (a) Schematic illustration of Mo catalytic oxidation of $O_2^{\bullet-}$ to $^1O_2$. Adapted with permission from ref. 43 Copyright (2021) American Chemical Society. (b) Schematic illustration of the generation of $^1O_2$ over $Fe_2O_3$@FCNT-H/$H_2O_2$. Adapted with permission from ref. 151 Copyright (2019) National Academy of Sciences.

the yield of $^1O_2$.[43,153] Sels *et al.* prepared a catalyst containing $MoO_4^{2-}$ exchanged on LDH to efficiently produce $^1O_2$ from $H_2O_2$.[154] Yi *et al.* developed a molybdenum (Mo) co-catalytic Fenton system and revealed that the exposed $Mo^{6+}$ can oxidize $O_2^{\bullet-}$ to $^1O_2$ in a Fenton-like reaction (Fig. 9a).[43] Intriguingly, Yang *et al.* built a catalyst with ~2 nm $Fe_2O_3$ nanoparticles distributed inside multiwalled carbon nanotubes (CNTs) to selectively activate $H_2O_2$ to give $^1O_2$ (Fig. 9b).[151] The Fe(III) species on the surface of the $Fe_2O_3$ inside the CNT is reduced by $H_2O_2$ to produce $HO_2^{\bullet}/O_2^{\bullet-}$, which is then oxidized to give $^1O_2$ in two pathways: (i) oxidation by Fe(III) in the favored spin state, and (ii) radical–radical reactions including the recombination of $HO_2^{\bullet}/O_2^{\bullet-}$ (the Gibbs free energy for the $HO_2^{\bullet}/O_2^{\bullet-}$ recombination reaction is −6.4 kcal $mol^{-1}$ at pH = 7). Defect structures may boost the generation of $^1O_2$ from $H_2O_2$. Li *et al.* disclosed the production of $^1O_2$ through rapid radical reactions in the vacancies of Fe–Co Prussian blue analogues.[155] Chong *et al.* found in the $FeCeO_x$–$H_2O_2$ Fenton-like system that the OVs on the metal oxide surface can participate in the $H_2O_2 \rightarrow {}^1O_2$ conversion to give $^1O_2$ as the primary ROS.[156]

**3.3.2 From $O_2$.** Energy transfer from the catalyst to the ground state oxygen ($^3O_2$) may give $^1O_2$.[157] Anionic vacancies on catalysts can serve as active sites to chemically adsorb $O_2$ and generate $^1O_2$.[136] Wang *et al.* found that OVs in OVs-$Bi_2O_3$ favor the activation of $O_2$ to form $^1O_2$ in the dark.[158] Calculations show that $O_2$ is chemically adsorbed on the surface of OVs-$Bi_2O_3$ but only physically adsorbed on pristine $Bi_2O_3$. The O=O bond length and the $O_2$ adsorption energy are 1.51 Å and 0.5 meV for $O_2$ on pristine $Bi_2O_3$, but 1.23 Å and 1.66 meV for $O_2$ on OVs-$Bi_2O_3$ (Fig. 10a and b). The $O_2$ adsorbed on OVs-$Bi_2O_3$ can be activated to the excited state (*i.e.*, $^1O_2$) because both the $\pi^*\uparrow$ and $\pi^*\downarrow$ states of $O_2$ are occupied (Fig. 10e and f).[158] Upon light irradiation, a faster generation of $^1O_2$ occurs over OVs-$Bi_2O_3$ compared with pristine $Bi_2O_3$, and OVs-$Bi_2O_3$ displays stronger capability on $O_2$ activation and thus a higher $^1O_2$ generation rate (Fig. 10c and d). However $^1O_2$ is the only ROS over OVs-$Bi_2O_3$; the OVs-free $Bi_2O_3$ produces other ROS (*e.g.*, $H_2O_2$ and $HO^{\bullet}$) along with $^1O_2$.[158] Ji *et al.* ultrasonically treated commercial $CoS_2$, and the SVs in the resulting deficient $CoS_{2-x}$ can tune the redox reaction on the $CoS_{2-x}$ surface to release $^1O_2$ in a sustained manner.[159] As abundant electrons are confined in the vacant electron orbitals of the SVs, $O_2$ can capture electrons from the SVs to form $O_2^{\bullet-}$ through a one-electron process (eqn (10)) or form $H_2O_2$ through a two-electron process (eqn (11)). $O_2^{\bullet-}$ can be quickly oxidized to $^1O_2$ by the highly oxidative $Co^{4+}$ or $Co^{3+}$ exposed on the S deficient surface (eqn (12)).

$$O_2 + e^- \text{ (defect)} \rightarrow O_2^{\bullet-} \quad (10)$$

$$O_2 + 2e^- \text{ (defect)} \rightarrow H_2O_2 \quad (11)$$

$$O_2^{\bullet-} + Co^{4+} \text{ (or } Co^{3+}) \rightarrow {}^1O_2 + Co^{2+} \quad (12)$$

**3.3.3 From PMS and PDS.** With traditional catalysts, the generation of $SO_4^{\bullet-}$ and $HO^-$ is the dominant process in the activation of PMS, and the production of $O_2^{\bullet-}$ and $^1O_2$ is just a competing process. However, with a suitable catalyst, the activation of PMS may also selectively generate $^1O_2$ and $O_2^{\bullet-}$ (Fig. 11b).[160] The activation energy for the self-decomposition of PMS in water to give $^1O_2$ ($HSO_5^- + SO_5^{2-} \rightarrow SO_4^{2-} + HSO_4^- + {}^1O_2$) is low,[161,162] but the rate constant of this reaction is also low (0.2 $M^{-1}$ $s^{-1}$) and the selective generation of $^1O_2$ is thus challenging. In activating PMS, OVs with localized electrons serve as the active sites for the heterolysis of PMS to generate $^1O_2$.[163] The OVs in the oxides can decrease the adsorption energy of PMS, elongate and weaken its O–O bond, and accelerate the decomposition process.[164] Zeng *et al.* activated PMS with OV-rich CoAl hydroxide@hydrosulfide to give $^1O_2$ as the main ROS to degrade sulfamethoxazole.[165] Zhao *et al.* found that the OV-rich $AgFe_{1-x}Ni_xO_2$ selectively activates PMS into $O_2^{\bullet-}$ and $^1O_2$ rather than $SO_4^{\bullet-}$ or $HO^{\bullet}$.[166] Compared with $AgFeO_2$ having a relatively perfect lattice, the OV-rich $AgFe_{1-x}Ni_xO_2$ has a more suitable redox potential for interacting with PMS and thus

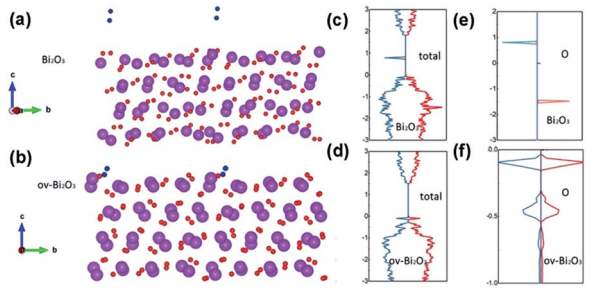


Fig. 10 Comparison of $O_2$ adsorption on the (120) surface of (a) pristine $Bi_2O_3$ and (b) OVs-$Bi_2O_3$ ($O_2$, blue; O atom of $Bi_2O_3$, red; Bi, purple); the total DOS of (c) $Bi_2O_3$ and (d) OVs-$Bi_2O_3$ with $O_2$; and partial DOS plot for $O_2$ absorbed on (e) $Bi_2O_3$ and (f) OVs-$Bi_2O_3$ surface; the up-spin states are represented by red curves and the down-spin states by blue curves. Adapted with permission from ref. 158 Copyright (2020) Wiley-VCH Verlag GmbH & Co. KGaA. Adapted with permission from ref. 159 Copyright (2021) Wiley-VCH Verlag GmbH & Co. KGaA.

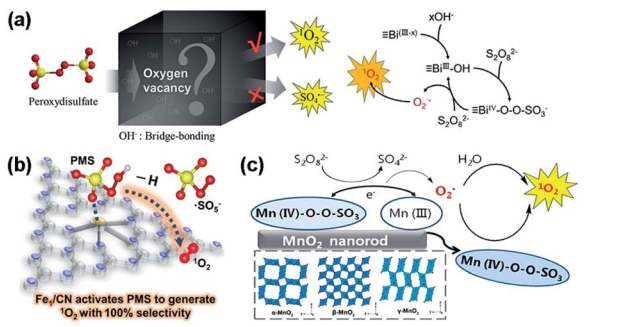


Fig. 11 (a) Proposed mechanism of OVs-mediated activation of peroxydisulfate to create $^1O_2$. Adapted with permission from ref. 168 Copyright (2021) American Chemical Society. (b) Schematic illustration of how the Fe single-atom catalyst ($Fe^1$/CN) activates PMS to generate $^1O_2$. Adapted with permission from ref. 160 Copyright (2021) Wiley-VCH Verlag GmbH & Co. KGaA. (c) Activation of PDS over manganese oxides. Adapted with permission from ref. 169 Copyright (2018) American Chemical Society.

 

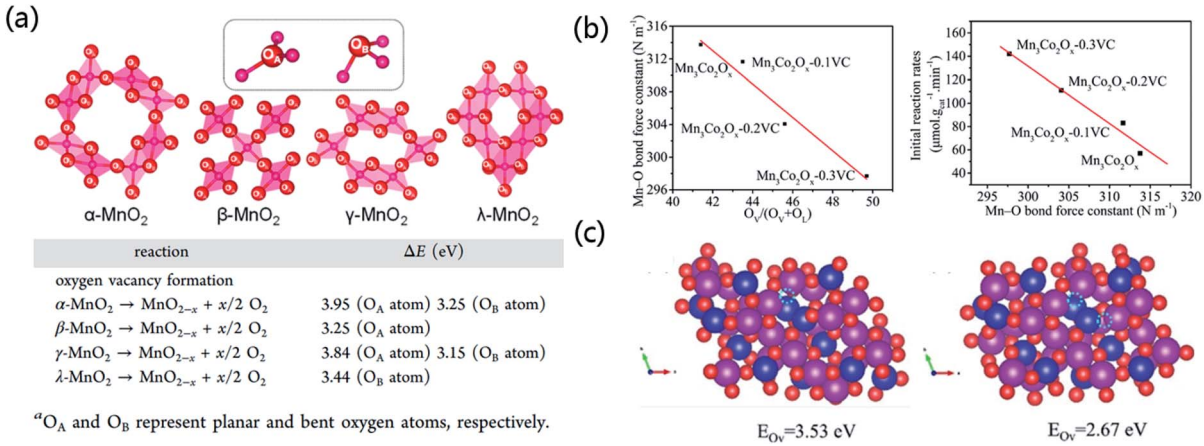


Fig. 12 (a) Calculated OV formation energies of $MnO_2$ of distinct phase structures. Adapted with permission from ref. 172 Copyright (2019) American Chemical Society. (b) Relationship between the Mn–O bond force constant and the relative OV content and the initial reaction rates of various $Mn_3Co_2O_x$–zVC catalysts. (c) Top views of the (111) plane of the Mn–Co spinel oxide with one OV and two neighboring OVs. Adapted with permission from ref. 173 Copyright (2021) American Chemical Society.



a lower energy barrier for the decomposition of PMS. Gao *et al.* reported that the evolution of $^1O_2$ over perovskite is well correlated with the OV concentration.[167] The activation energies of PMS self-decomposition to give $^1O_2$ are 48.4, 22.6, and 15 kJ $mol^{-1}$ for $LaFeO_3$, $LaFe_{0.6}Zn_{0.4}O_3$, and $LaMnO_3$, respectively.

Bu *et al.* activated PDS to generate $^1O_2$ on the deficient surface of BiOBr.[168] The OVs of BiOBr interact with hydroxyl ions ($HO^-$) to form $Bi^{III}$–OH species, which are the major active sites for the adsorption and activation of PDS. The PDS adsorbed at the $Bi^{III}$–OH sites produces the metastable $Bi^{IV}$–$O^{(-1)}$–$O^{(-1)}$–$SO_3^-$ intermediate, which reacts with another PDS to release $O_2^{\bullet-}$ when the $Bi^{IV}$–O bond breaks. In this process, the O atom bonded to $Bi^{IV}$ acts as the electron donor, and $Bi^{IV}$ acts as the electron acceptor. Finally, $Bi^{(IV-x)}$–$O^{(-1)}$–$O^{(-1)}$–$SO_3^-$ reacts with $O_2^{\bullet-}$ to produce $^1O_2$ under alkaline conditions (Fig. 11a).

Many studies have suggested the direct oxidation of $O_2^{\bullet-}$ as a common route to generate $^1O_2$,[43,169,170] and the oxidation of $O_2^{\bullet-}$ to $^1O_2$ requires an oxidant with a redox potential of at least 0.34 V *vs.* NHE. Hu *et al.* revealed that the OV concentration of $Co_3O_4$ impacts its efficiency in activating PMS to give $^1O_2$.[171] The PMS decomposition mainly depends on the adsorption energy of PMS on the $Co_3O_4$ surface, the cleavage of the O–O bond in the PMS molecule, and the electron transfer between PMS and $Co_3O_4$. The direct oxidation of $O_2^{\bullet-}$ to give $^1O_2$ may account for the generation of $^1O_2$ in view of the thermodynamics, *i.e.*, $E_0$ ($Co^{3+}/Co^{2+}$) = 1.93 V and $E_0$ ($O_2^{\bullet-}/^1O_2$) = −0.34 V. Prior studies have also shown that the oxidization of $O_2^{\bullet-}$ to $^1O_2$ is thermodynamically feasible with $Cu^{III}$ and $Mn^{IV}$ (Fig. 11c),[169,170] as $E_0$ ($Cu^{III}/Cu^{II}$) = 2.3 V *vs.* NHE and $E_0$ ($Mn^{IV}/Mn^{III}$) = 0.95 V *vs.* NHE. The reduction of $Mo^{6+}$ by $O_2^{\bullet-}$ during the Fenton reaction can also give $^1O_2$, *i.e.*, $Mo^{6+} + O_2^{\bullet-} \rightarrow {}^1O_2 + Mo^{4+}$.[43]

### 3.4 Lattice oxygen in TMO: reactivity and regeneration

Just like $HO^\bullet$, $O_2^{\bullet-}$ and $^1O_2$, the $O_L$ of TMO itself can also serve as the ROS to participate in AOPs. Since $O_L$ already exists stably in TMO, it is not newly generated from a precursor, but it needs to be constantly replenished in the oxidation reaction as described in the MvK mechanism. TMO with highly reactive $O_L$ generally have low OV formation energy that arises from a weak M–O bond and strong oxygen migration ability in the TMO lattice.[104] Hayashi *et al.* found that β- and λ-$MnO_2$ are good catalysts for the oxidation of hydroxymethyl furfural (HMF).[172] Compared with α- and γ-$MnO_2$, β- and λ-$MnO_2$ have lower OV formation energies due to their distinct crystal structures, and for both α- and γ-$MnO_2$ the OV formation energies are higher at the planar oxygen sites than at the bent oxygen sites (Fig. 12a).

The OVs of deficient TMO can regulate the coordination structure of the TMO and alter the reactivity of $O_L$.[103] Liu *et al.* presented a facile and green vitamin C-assisted solid-state grinding method to synthesize mesoporous Mn–Co spinel oxides with a well-defined OV concentration.[173] The Mn–Co oxides with a higher OV concentration have a weaker Mn–O bond and higher $O_L$ reactivity (Fig. 12b). According to DFT calculations and *in situ* FT-IR studies, the removal energy of $O_L$ decreases significantly from 3.53 to 2.67 eV when there is an adjacent OV (Fig. 12c). That is, the $O_L$ becomes more active when OVs exist in its surrounding. The analyses of Raman spectroscopy, $H_2$-TPR, and $O_2$-TPD show that the $Mn_3Co_2O_x$–0.3VC catalyst with a higher OV concentration has stronger $O_L$ reactivity than $Mn_3Co_2O_x$.

Doping is a common strategy to enhance the reactivity of $O_L$, as doping TMO with cations (*e.g.*, $Li^+$, $Mg^{2+}$, $Ca^{2+}$, $Sr^{2+}$, $Al^{3+}$, $Zn^{2+}$, and $Ln^{3+}$) can decrease the OV formation energy. Low-valence dopants may create OVs and enhance the reactivity of $O_L$.[27] Xu *et al.* prepared $Li^+$-doped NiO which has remarkably enhanced $O_L$ reactivity than pristine NiO.[174] The OV formation energy is 3.32 eV for pure NiO but only 2.12 eV for $Li^+$-doped NiO. Schlexer *et al.* introduced Au to $TiO_2$ to capture the excess electrons associated with the vacancies formed at the Au/$TiO_2$ perimeter to stabilize the vacancies.[175] The OV formation energy at the Au/$TiO_2$ perimeter is reduced by 1.32 eV with respect to

the Au-free surface. Dostagir *et al.* prepared a catalyst with isolated Co atoms in $ZrO_2$ and demonstrated with DFT calculations that the OV formation energy of $ZrO_2$ is decreased by Co doping to between −1.45 and −1.17 eV from 2.70–3.20 eV.[176] That is, OV formation is endothermic on pure $ZrO_2$ but becomes exothermic after Co doping. OV sites are created near Co atoms due to mismatch in the oxidation states of $Co^{2+}$ and $Zr^{4+}$ and thus facilitate the need for charge balance.

Doping may also enhance the $O_L$ reactivity by inducing structural distortion in the oxides. Zhao *et al.* found that the Raman peaks of Ni-doped $Co_3O_4$ shift to lower frequencies and become broader because lattice distortion weakens the Co–O bond.[177] Consequently, more OVs are created in the oxide, the $O_L$ has stronger mobility, and the active surface $O_L$ become more abundant. Zhang *et al.* showed that the [$FeO_6$] octahedral distortion in $La_{1-x}Ce_xFeO_3$ promotes the mobility and reactivity of $O_L$,[178] suggesting that it is feasible to tailor the reactivity of $O_L$ in perovskites by modulating the distortion of $BO_6$ in $ABO_3$ (Fig. 13a).

The efficient regeneration of $O_L$ can also benefit from OVs. OVs can enhance the adsorption of $O_2$ and the storage of $O_2^{2-}$ on the TMO surface in the MvK process.[180] Lu *et al.* incorporated Fe into CuO–$CeO_2$ to create the Fe–O–Ce structure with rich OVs and measured *in situ* the oxygen storage capacity (OSC) of the oxides by the CO pulse technique.[181] The OVs readily trap the $O_2$ in the gas phase, which ensures a durable release of subsurface lattice oxygen to supply reactive $O_L$. The initial CuO–$CeO_2$ catalyst has a low OSC value of 46.4 μmol $CO_2$ per g, whereas the Fe-doped CuO–$CeO_2$ has a considerably higher OSC value of 94.8 μmol $CO_2$ per g thanks to the greater number of OVs introduced by Fe doping. Similarly, Wang *et al.* assembled ultrathin and vacancy-rich CoAl-LDH nanosheets prepared from exfoliating bulk CoAl-LDH with graphite oxide (GO) to obtain the CoAl-ELDH/GO hybrid catalyst that possesses abundant newly generated OVs.[182] The OVs promote oxygen adsorption and storage over the deficient CoAl-ELDH/GO, which has larger $O_2$-TPD peaks than the corresponding bulk CoAl-LDH. Yang *et al.* showed with DFT calculations that $O_2$ can be strongly adsorbed and activated on the defective Mn-doped c-$ZrO_2$ (111) surface with OVs.[179] The OVs elongate the O═O bond from 1.24 Å on the perfect Mn-doped c-$ZrO_2$ (111) surface to 1.37 Å on the defective surface. The OV formation energy and the adsorption energy of $O_2$ are 5.84 eV and 0.37 eV on the perfect *m*-$ZrO_2$ (−111) surface, 0.18 eV and −0.05 eV on the perfect Mn-doped c-$ZrO_2$ (111) surface, and down to 0.18 eV and −0.74 eV on the defective Mn-doped c-$ZrO_2$ (111) surface, respectively (Fig. 13b).

Generally, there are two possible pathways (*i.e.*, $R^1$ and $R^2$ mechanism) for the gas phase $O_2$ to oxidize the OVs and replenish $O_L$. In the $R^1$ mechanism, the exchange of oxygen species occurs at one surface vacant site. In the $R^2$ mechanism, two adjacent surface vacant sites are needed to adsorb and decompose the gaseous $O_2$. Feng *et al.* ran isotopic $^{18}O_2$ tracing experiments and demonstrated that the adsorption and activation of gas phase $O_2$ on $Bi_2B_2O_7$ mainly follow an $R^2$ mechanism that requires two adjacent surface vacancies (Fig. 13c).[102]

### 3.5 Tailoring the reactive oxygen species generation

PMS, PDS and $H_2O_2$ are strong oxidants but normally have low reaction rates with most organic pollutants. Catalysts bearing transition metal ions (*e.g.*, Fe, Mn, Co, Ni, V, Ce, *etc.*) are promising activators for these oxidants to give powerful ROS.[183] Transition metal catalysts can provide a diversity of metals with tunable valence states to afford high redox properties, and an appropriate d-band center to balance the catalyst-adsorbate binding strength, as well as controllable surface and electronic structures to promote light absorption and/or adsorbate adsorption, all crucial for tailoring and boosting the generation

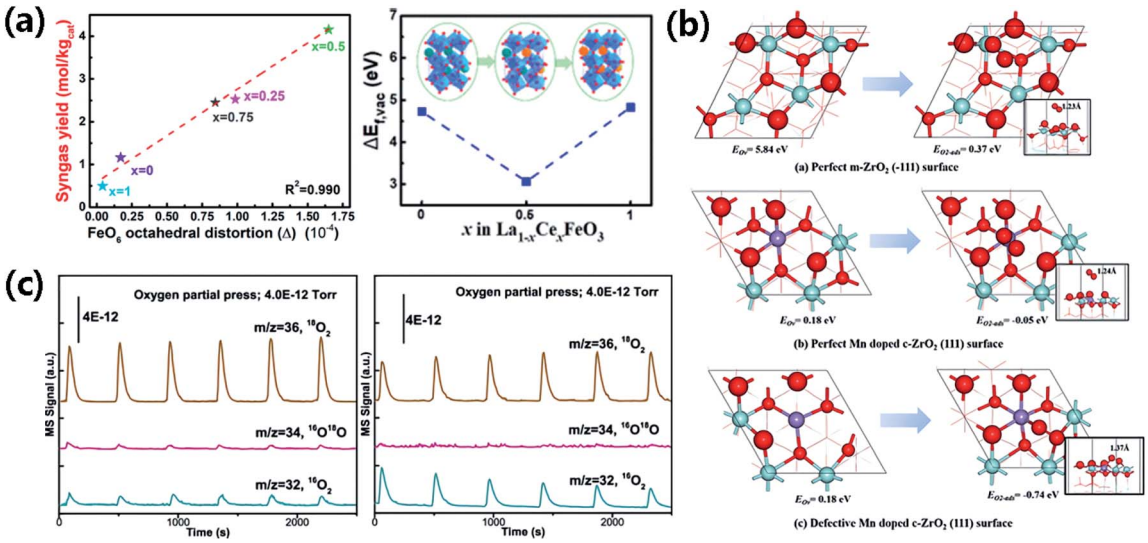


Fig. 13 (a) The OV concentration and possible reaction mechanism of POM-$CO_2$ splitting over $La_{1-x}Ce_xFeO_3$ ($x$ = 0, 0.5, 1). Adapted with permission from ref. 178 Copyright (2020) American Chemical Society. (b) OV formation energy ($E_{Ov}$) and adsorption energy of $O_2$ ($E_{O}2_{-ads}$) over distinct Zr sites. Adapted with permission from ref. 179 Copyright (2018) American Chemical Society. (c) Isotopic $^{18}O_2$ exchange analysis of $Bi_2Zr_2O_7$ at 300 °C and 400 °C. Adapted with permission from ref. 102 Copyright (2021) American Chemical Society.

 

of ROS. Note that the catalysts containing different types of transition metals are frequently found to give the same type of ROS.[16,184–186] Hence, it should not just be the type of transition metal ions controlling the selectivity and efficiency of ROS generation.[187] Recent studies have shown that modulation of the geometrical and electronic structures of catalysts is a key to probe how to customize the ROS production.

Tuning the geometrical structure of catalysts can change the binding effect of catalysts and oxidants and monitor the ROS generation. For instance, transition metal based catalysts commonly drive the dissociation of PMS and PDS into $SO_4^{\bullet-}$ and $HO^{\bullet}$.[169] It has been reported that the catalysts of $CoN_4$ structure prefer to adsorb the O atom connected to S in the PMS, and the system produces a mixture of ROS including $SO_4^{\bullet-}$, $HO^{\bullet}$, $O_2^{\bullet-}$ and $^1O_2$.[188,189] In comparison, when Co is coordinated with N to form a $CoN_{[2+2]}$ structure, $CoN_{[2+2]}$ can bind the O from –OH in the PMS, while the loss of the H atom of –OH creates a $SO_5^{\bullet-}$ intermediate.[188,189] Since $SO_5^{\bullet-}$ has a high reaction rate ($\sim 2 \times 10^8$ $M^{-1}$ $s^{-1}$) and low activation energy (7.4 $\pm$ 2.4 kcal $mol^{-1}$), it can rapidly transfer into $^1O_2$ *via* eqn (13)–(15).[188,189] Intriguingly, on the deficient surface of BiOBr the PDS can be activated into $^1O_2$.[168] The OVs of BiOBr interact with $HO^-$ to form $Bi^{III}$–OH species and produce the $Bi^{IV}$–$O^{(-1)}$–$O^{(-1)}$–$SO_3^-$ intermediate, which reacts with another PDS to release $O_2^{\bullet-}$, while $Bi^{(IV-x)}$–$O^{(-1)}$–$O^{(-1)}$–$SO_3^-$ reacts with $O_2^{\bullet-}$ to produce $^1O_2$ under alkaline conditions (Fig. 11a).

$$HSO_5^- \rightarrow SO_5^{\bullet-} + H^+ + e^- \quad (13)$$

$$SO_5^{\bullet-} + SO_5^{\bullet-} \rightarrow S_2O_8^{2-} + {}^1O_2 \quad (14)$$

$$SO_5^{\bullet-} + SO_5^{\bullet-} \rightarrow 2SO_4^{2-} + {}^1O_2 \quad (15)$$

Tuning the electronic structure of photocatalysts can boost the generation and transfer of electrons for catalytic reactions. Wu *et al.* employed OVs to mediate $^1O_2$ generation in the Fe–Co LDH/PMS system, and found that PMS tends to donate one electron to the OV and is thus activated to form $^1O_2$.[190] When oxidation reactions involve photocatalytic reactions, a key to tailor ROS generation is by tuning the band and electronic structure of photocatalysts. Introducing point defects (*e.g.* OVs) could create additional defect levels of photocatalysts, rendering a downshift of the conduction band (CB) minimum, and/or an upshift of the valence band (VB) maximum.[143,144] With an appropriate band structure, the electrons in the defect levels could transfer to the CB band through inter-band excitation and be captured by $O_2$ that generates $O_2^{\bullet-}$,[191] while upshift of the VB band may help suppress the oxidation of $H_2O$ to $HO^{\bullet}$. For instance, CdS and $ZnIn_2S_4$ catalysts have appropriate conduction and valence bands for $O_2^{\bullet-}$ generation while avoiding $HO^{\bullet}$ generation.[192] The presence of OVs could introduce intermediate energy states, leading to a narrowed band gap and enhanced charge carrier separation efficiency,[193,194] and helps extend the light response to visible or even near infrared light,[195,196] Wang *et al.* showed that OV-rich sulfur-doped BiOBr has a narrowed band gap responsible for the visible light and can generate $O_2^{\bullet-}$ and $HO^{\bullet}$ efficiently for 4-chlorophenol degradation.[197]

To date, it remains an open question to establish robust principles to develop effective transition-metal-based catalysts for fine control over ROS generation. The roles and mechanism responses of different metal groups in distinct reaction pathways await to be disclosed, by performing more systematical investigations under the assistance of operando spectroscopic studies and theoretical calculations.

# 4 Detection of reactive oxygen species

## 4.1 Hydroxyl radical

**4.1.1 EPR measurement.** The spin trapping method is a common method to detect ROS. Electron Paramagnetic Resonance (EPR) is a useful and facile method for the direct detection of free ROS at concentrations as low as 1 μM.[198] DMPO (5,5-dimethyl-1-pyrroline noxide) often severs as a trapping reagent to convert $HO^{\bullet}$ into more stable DMPO-$HO^{\bullet}$,[199] which displays quartet EPR signals with a relative intensity of 1 : 2:2 : 1.[200]

**4.1.2 Spectroscopic measurement.** Spectroscopic detection strategies, including absorbance (UV/Vis), fluorescence (FL) and chemiluminescence (CL), offer an alternative approach to identify ROS.[201] Simple molecules such as terephthalic acid,[202] coumarin[203] and carboxyl derivatives of coumarin[204] are normally employed to detect $HO^{\bullet}$ as they can generate the corresponding fluorescent derivate in solution. For instance, $HO^{\bullet}$ can react with terephthalic acid to produce 2-hydroxyterephthalic acid (TAOH),[205] and the amount of $HO^{\bullet}$ is quantified by analyzing the fluorescence intensity of TAOH ($\lambda_{exc}$ = 320 nm; $\lambda_{em}$ = 420 nm). Likewise, the coumarin (COU) and coumarin-3-carboxylic acid (3-CCA) reacting with $HO^{\bullet}$ produce fluorescent derivates, *i.e.*, 7-hydroxy-coumarin ($\lambda_{exc}$ = ~320–370 nm; $\lambda_{em}$ = ~450 nm) and 7-hydroxy-3-carboxycoumarinic acid ($\lambda_{exc}$ = ~380–400 nm; $\lambda_{em}$ = ~450 nm), respectively.[206]

## 4.2 Superoxide radical

**4.2.1 EPR measurement.** DMPO (5,5-dimethyl-1 pyrroline N-oxide) can also serve as the trapping reagent to detect $O_2^{\bullet-}$ in aqueous solution during ESR measurements. DMPO-$O_2^{\bullet-}$ normally displays an EPR signal with four major peaks of a relative intensity of 1 : 1:1 : 1.[207] As the reaction rate of DMPO with $O_2^{\bullet-}$ is much slower than that with $HO^{\bullet}$ in aqueous solution, and DMPO-$O_2^{\bullet-}$ is more stable than DMPO-$HO^{\bullet}$ in methanol,[208] it is preferred to perform the EPR measurements of $O_2^{\bullet-}$ in methanol solvent.

**4.2.2 Spectroscopic measurement.** Additives such as nitro blue tetrazolium (NBT, 2,2′-di-*p*-nitrophenyl-5,5′-diphenyl-(3,3′-dimethy)-4,4′-bisphenyleneditetrazolium chloride) could be applied to detect $O_2^{\bullet-}$.[33] $O_2^{\bullet-}$ can react with yellow NBT to create blue formazan, leading to the decrease of the absorption peak of NBT at 260 nm in UV-visible spectra, as an indicator of the amount of $O_2^{\bullet-}$.[209,210] Luminol and MCLA (6-(4-methoxyphenyl)-2-methyl-3,7-dihydroimidazo-[1,2-*a*]pyrazin-3-one hydrochloride) can also be used to trace $O_2^{\bullet-}$ *via* chemiluminescence (CL) analysis,[211,212] and the CL strategy could detect the trace amount of $O_2^{\bullet-}$.[212]

### 4.3 Singlet oxygen

**4.3.1 EPR measurement.** Sterically hindered cyclic amines can react with $^1O_2$ to generate the 1-oxyl radical for identifying $^1O_2$ in EPR analysis. For instance, 2,2,6,6-tetramethylpiperidine (TEMP) reacting with $^1O_2$ gives a stable nitroxide radical (2,2,6,6-tetramethylpiperidine 1-oxyl, TEMPOL),[213] which displays EPR spectra with a 1 : 1 : 1 triplet signal.[214] For the detection of $^1O_2$, the use of 4-oxo-tetramethylpiperidine,[215] and 4-hydroxy-tetramethylpiperidine[216] has also been reported.

**4.3.2 Spectroscopic measurement.** Both fluorescence and colorimetric methods can be used to detect $^1O_2$. A singlet oxygen sensor green (SOSG) having a weak blue fluorescence peak with $\lambda_{em}$ = 395 nm at $\lambda_{exc}$ = 372 nm, and $\lambda_{em}$ = 416 nm at $\lambda_{exc}$ = 393 nm can be used for $^1O_2$ detection. The reaction of $^1O_2$ with SOSG produces endoperoxide that gives green fluorescence with $\lambda_{em}$ = 525nm at $\lambda_{exc}$ = 504 nm.[217] Besides, researchers have confirmed that 1,3-diphenylisobenzofuran (DPBF) can react with $^1O_2$ giving endoperoxide (DPBF-EP),[218] and the amount of $^1O_2$ is proportional to the decrease of DPBF which has absorption intensity at about 410 nm in UV-vis spectroscopy analysis.[219,220]

### 4.4 Quenching technique

When two or more ROS are generated over the catalyst, a quenching experiment can be employed to identity the dominant ROS in the AOP system. Since many alcohols (*e.g.*, isopropanol (IPA),[221] mannitol,[222] *t*-butyl alcohol (TBA)[223] and methanol[224]) can efficiently react with HO$^\bullet$, these substances could be good candidate reagents to quench HO$^\bullet$. It is worth noting that methanol can also work as the scavenger for quenching $SO_4^{\bullet-}$,[225] while TBA is only effective for quenching OH$^\bullet$ but not for $SO_4^{\bullet-}$.[226]

Benzoquinone (BQ),[227,228] ascorbic acid,[228] superoxide dismutase (SOD)[229] and trichloromethane[230] can be used to remove $O_2^{\bullet-}$ in oxidation reactions. For instance, in many cases, $O_2^{\bullet-}$ may serve as an intermediate for the generation of other ROS (*e.g.*, $^1O_2$). To find out whether $O_2^{\bullet-}$ is the intermediate of $^1O_2$ or the dominant ROS for pollutant degradation, Yi[43] and Zhang[189] introduced BQ as a quenching agent of $O_2^{\bullet-}$, and showed that $O_2^{\bullet-}$ served as an intermediate to form $^1O_2$, the active species in their studies.

Useful quenching agents for $^1O_2$ include $NaN_3$,[231] furfur alcohol (FFA),[232] L-tryptophan[233] *etc.* However, since FFA or $NaN_3$ can also react with free radicals,[234] it is infeasible to use FFA/$NaN_3$ as a scavenger when the oxidation system contains both the radical and non-radical ROS. In addition, $NaN_3$ can react with PMS rapidly, and hence, it cannot apply to the PMS-involved system. Besides the quenching technique, sometimes, the solvent exchange method that replaces $H_2O$ by $D_2O$ can help identity the generation of $^1O_2$, as the lifetime of $^1O_2$ in $D_2O$ is about ~55 μs, more than 10 times that (~4.2 μs) in $H_2O$.[235,236]

## 5 Reactions of reactive oxygen species

### 5.1 Hydroxyl radical

**5.1.1 Scavenging pollutants.** Because of its high oxidation potential, HO$^\bullet$ can react with the strong bonds of persistent organic matter (*e.g.*, C–H bond in benzene) and oxidize tropospheric trace species or pollutants to $CO_2$ and $H_2O$.[237,238] It can react at a relatively fast rate with easily oxidizable organic compounds (*e.g.*, methylene blue, promazine, and promethazine) through one-electron abstraction,[239] or at a relatively slower reaction rate with saturated hydrocarbons (*e.g.*, aliphatic compounds without double C=C bonds) by abstracting hydrogen atoms.[240] Because of its electrophilic nature, HO$^\bullet$ prefers to react with the C=C and C=N bonds in the organic substrate rather than the C=O bond whose carbon atom is electron-deficient.[39] Nevertheless, it can react with aliphatic carboxylic acids to create highly reactive carbon-centered radicals *via* abstraction of the hydrogen atom, and react with aromatic carboxyl acids *via* hydroxylation.

The surface defects of TMO can effectively enhance the oxidation performance of HO$^\bullet$. For instance, the Co–Cu LDH with abundant OVs can boost the dissociation of $H_2O_2$ to generate a sufficient amount of HO$^\bullet$ for the degradation of anthraquinones.[241] The highest COD and TOC removal values (89.9% and 71.3% respectively) are achieved with an initial $H_2O_2$/TOC ratio of 75 and an initial pH of 6.8. Zhang *et al.* examined a ceria-based heterogeneous Fenton-like catalyst.[242] Compared with pure iron oxide and ceria, Fe-doped $CeO_2$ with abundant OVs ($FeCeO_x$) degrades rhodamine B (RhB) at a higher efficiency (98%) over a wider working pH range (3.0–9.0). The surface HO$^\bullet$ is the predominant ROS to oxidize RhB. Annealing the $FeCeO_x$ in an oxygen atmosphere eliminates the OVs, and the annealed $FeCeO_x$ with fewer OVs has poorer performance in activating $H_2O_2$ and degrading the target pollutant. Zhan *et al.* prepared OV-rich Co–ZnO microparticles (OV–CoZnO MPs) as a Fenton-like catalyst.[119] The electron-rich OV sites on the catalyst are the key active sites responsible for the capture and reduction of $H_2O_2$ to generate HO$^\bullet$ to degrade organic pollutants (*e.g.*, BPA, PHT, 2,4-D, phenol, and methylene blue) over a wide pH range (4.5–9.5). In addition, the electron-deficient $Co^{3+}$ sites of the catalyst appear to actively adsorb the pollutant, and the organic pollutant adsorbed on $Co^{3+}$ acts as an electron donor to further accelerate the degradation process. The OV-CoZnO MPs/$H_2O_2$ system with dual reaction centers can degrade pollutants about ~17 times faster than the ZnO/$H_2O_2$ system that has only one reaction center.

Li *et al.* performed quantitative analysis and reported an interesting case that shows the selectivity of HO$^\bullet$ in the degradation of pollutants (Fig. 14e and f).[243] The OVs of the BiOCl catalyst demonstrate an electron donor nature and serve as the "Fenton-catalytic" center to dissociate $H_2O_2$ to generate HO$^\bullet$, but it occurs in a surface confinement pathway. The generated HO$^\bullet$ quickly diffuses away from the (001) surface of BiOCl, because the steric hindrance due to the high density of O atoms on the (001) surface prevents the binding of newly generated HO$^\bullet$ (Fig. 14a–d). However, free HO$^\bullet$ prefers to oxidize dissolved pollutants (*e.g.*, benzoic acid, benzene, and phenol) in the solution (Fig. 14g); the nascent HO$^\bullet$ on the (010) surface of BiOCl prefers to bond and stay on the catalyst surface to react with strongly adsorbed pollutants (*e.g.*, formic acid, rhodamine B, and methyl orange) (Fig. 14g).

 

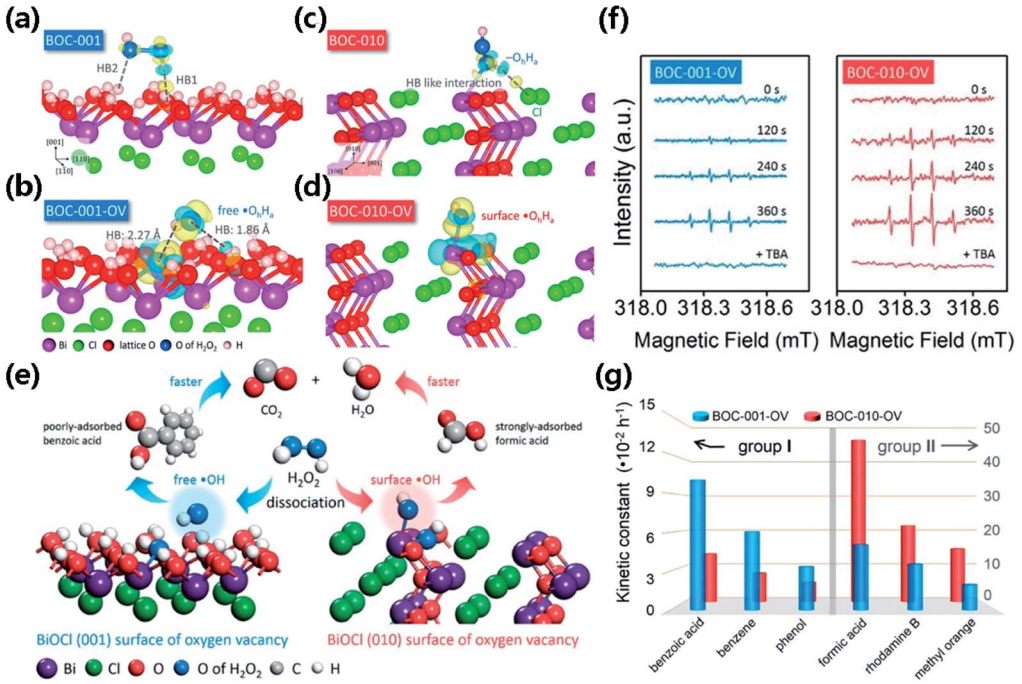


Fig. 14 Schematic illustration of $H_2O_2$ dissociation on (a) BOC-001, (b) BOC-010, (c) BOC-001-OV and (d) BOC-010-OV, respectively. (e) Schematic illustration of $H_2O_2$ dissociation on different surfaces of BiOCl with OVs for scavenging benzoic acid and formic acid, respectively. (f) EPR spectra of spin-reactive HO$^{\bullet}$ radicals generated over BOC-001-OV and BOC-010-OV in the presence of $H_2O_2$, respectively. (g) Reaction kinetic constants of BOC-001-OV and BOC-010-OV for the removal of group I and group II pollutants. Adapted with permission from ref. 243 Copyright (2017) American Chemical Society.

**5.1.2 Generating value-added chemicals.** The selective oxidation of organic substrates to value-added products is of prime importance in organic synthesis but can require the use of expensive and toxic dichromate or permanganate reagents. Although HO$^{\bullet}$ typically mineralizes organic pollutants completely, it may also engage in selective oxidations to give value-added chemicals. For instance selective oxidation of alcohols to aldehydes remains one of the most important functional transformations in the synthesis of fine chemicals. Aldehydes such as benzaldehyde have been widely used in the synthesis of perfumes, dyes, and pharmaceuticals.[244] However, the selective oxidation of alcohols to aldehydes without over-oxidation to carboxylic acids remains challenging. Liu *et al.* found that photogenerated holes from the valence band of reconstructed carbon nitride nanosheets react with $OH^-$ to form HO$^{\bullet}$ as the ROS, which in turn selectively oxidizes phenylcarbinol to give phenyl methanal *via* radical intermediates.[245] Luo *et al.* used ultrathin Co-based LDH and graphene to modify $BiVO_4$ photoanodes to accomplish photoelectrochemical (PEC) water oxidation, where HO$^{\bullet}$ is generated to selectively oxidize benzyl alcohol to benzaldehyde (Fig. 15).[246] Isotope-labeling experiments reveal that HO$^{\bullet}$ is generated from the water oxidation reaction and binds to the LDH surface *via* hydrogen bonding. *In situ* electron spin resonance confirms that HO$^{\bullet}$ is the main ROS responsible for the selective oxidation of benzyl alcohol. In addition, FT-IR spectroscopy shows that the catalyst surface preferentially adsorbs benzyl alcohol and readily desorbs the generated benzaldehyde, which is helpful for selective oxidation.

## 5.2 Superoxide radical

**5.2.1 Scavenging pollutants.** Although $O_2^{\bullet-}$ is less reactive than HO$^{\bullet}$,[33] in recent years it has been frequently exploited as a green "aqua cleaner" for scavenging anthropogenic pollutants. Watts and coworkers pioneered in using $O_2^{\bullet-}$ to degrade halogenated pollutants.[248–250] Zhang *et al.* found that the direct degradation of *p*-nitrophenol involves $O_2^{\bullet-}$ rather than HO$^{\bullet}$ as the main ROS, and the degree of $O_2^{\bullet-}$ participation during the direct degradation mainly depends on the molecular structure of the pollutant.[251] The photocatalytic degradation of tetracycline over ZnO involves $O_2^{\bullet-}$ as the primary ROS, as it is generated at much higher concentrations than HO$^{\bullet}$ on the catalyst surface.[252]

As a free radical, $O_2^{\bullet-}$ can work as both an electron transfer agent and an electron acceptor.[253] Xiao *et al.* studied how the unpaired electrons fit into the resonance π* molecular orbitals in $O_2^{\bullet-}$ and found that the HOMO and LUMO of $O_2^{\bullet-}$ are degenerated.[254] Thus, $O_2^{\bullet-}$ is both electrophilic and nucleophilic, and can work as either a reducing agent or an oxidizing agent.[255,256] Because the carboxyl group is weakly electron-withdrawing and the hydroxyl group is electron-donating, the efficiency of degradation by $O_2^{\bullet-}$ ranks as hydroquinone < *p*-hydroxybenzoic acid < *p*-nitrophenol, which is the exact opposite order of their electron cloud density.[251]

Defect structures on the catalyst can help generate $O_2^{\bullet-}$ for AOP. In the degradation of ciprofloxacin over W-doped $CeO_2$, W is beneficial for the formation of surface OVs, and the deficient surface effectively adsorbs and activates $O_2$ to $O_2^{\bullet-}$ through

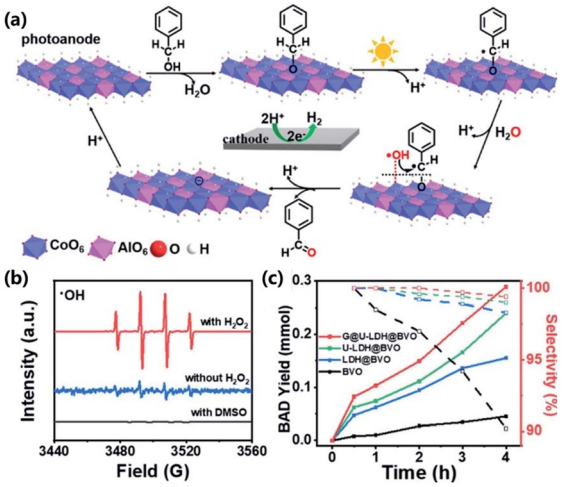


Fig. 15 (a) Mechanism of selective benzyl alcohol (BA) activation coupled with PEC water oxidation. (b) ESR spectra of HO$^{\bullet}$ generated over the graphene@ultrathin-CoAl-LDH@$BiVO_4$ under different conditions ($H_2O_2$, 30%, 0.1 mM; DMSO, 0.5 mM). (c) Benzaldehyde yield (solid squares and lines) and selectivity (empty squares and dashed lines) at different reaction times in the PEC oxidation of BA under illumination (AM 1.5G, 100 mW cm$^{-2}$) at 1.2 V *vs.* RHE. Solution: 2 mmol BA in PBS (pH = 7, 0.1 M, 10 mL) at 10 mV s$^{-1}$ scan rate. Adapted with permission from ref. 246 Copyright (2020) American Chemical Society.

a one electron transfer process.[257] The 2% W/$CeO_2$ can degrade ciprofloxacin in a wide pH range with excellent efficiency. In some cases, $O_2^{\bullet-}$ and other species in the reaction medium react with the substrate concurrently. For instance, in the oxidation of BPA over $AgFe_{1-x}Ni_xO_2$, the dominant ROS are $O_2^{\bullet-}$ and $^1O_2$, rather than the traditional $SO_4^{\bullet-}$ or HO$^{\bullet}$.[166] Analogously, the $MnO_2$-mediated degradation of anthracene is mediated by both the non-radical oxidation by $Mn^{3+}$ and the radical-based oxidation by $O_2^{\bullet-}$.[258]

It is worth remarking that the geometry of $O_2^{\bullet-}$ on the catalyst surface may affect the outcome of the oxidation reaction. Li *et al.* engineered deficient BiOCl that can oxidize NO completely into nitrate under visible light irradiation with >99% selectivity (Fig. 16a).[247] When the reaction is carried out at ambient temperature, the carefully crafted OVs on the prototypical (001) surface of BiOCl preferentially give $O_2^{\bullet-}$ in a side-on bridging mode and suppress the thermodynamically stable terminal end-on geometry that will be predominant at an elevated temperature (Fig. 16b–e). This newly developed $O_2^{\bullet-}$-mediated technique thus avoids the partial oxidation of NO to $NO_2$.

**5.2.2 Generating value-added chemicals.** Thanks to its moderate oxidation potential, $O_2^{\bullet-}$ allows the selective oxidation of organic substrates (*e.g.*, olefins, alcohols, and amines) to give valuable chemical products.[259–261] Ito *et al.* thermally oxidized styrenes to benzaldehydes with $H_2O_2$ over $TiO_2$ without additional light irradiation and found that the hydroperoxy radical ($^{\bullet}$OOH) and $O_2^{\bullet-}$ are responsible for the selective oxidation.[262] Xie *et al.* oxidized aliphatic alcohols to aldehydes with $O_2$ at room temperature and found that BiOCl attains >90% conversion and nearly 100% selectivity.[263] The BiOCl photocatalyst is excited to produce $h^+/e^-$ pairs. The adsorbed alcohol reacts with the photo-generated holes and subsequently deprotonates to form a carbon radical, which combines with $O_2^{\bullet-}$ to form aldehydes. The adsorbed protons decompose the C–O and O–O bond to form aldehyde and $H_2O_2$. Chen *et al.* employed OV-rich $Bi_2MoO_6$ to selectively oxidize benzyl alcohol with $O_2$ to produce both benzaldehyde and $H_2O_2$ simultaneously.[264] According to *in situ* ESR measurements, both carbon-centered radicals and $O_2^{\bullet-}$ are key intermediates. The concentration of OVs is readily tunable, and the rate of benzaldehyde formation is 1310 μmol g$^{-1}$ h$^{-1}$ with OV-rich $Bi_2MoO_6$, 2.3 times that of OVs-poor $Bi_2MoO_6$. The OVs on $Bi_2MoO_6$ accelerate charge separation and charge transfer, and they also enhance the adsorption and activation of both benzyl alcohol and $O_2$.

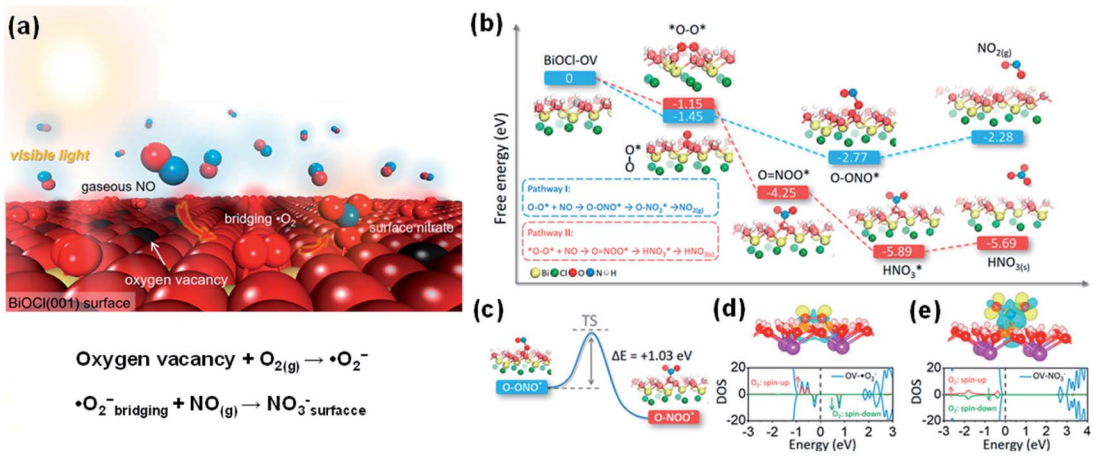


Fig. 16 (a) Schematic illustration of photocatalytic NO removal by BiOCl-OV. (b) Free energy change against the reaction coordinate for the oxidation of NO by $O_2^{\bullet-}$ on the BiOCl (001) surface in different geometries. (c) Geometric transition from peroxynitrite to nitrate. TS represents the transition state. Charge density difference and $O_2$ partial DOS of the BiOCl (001) surface adsorbed with (d) $O_2$ and (e) nitrate. The yellow and blue isosurfaces with an isovalue of 0.005 au represent charge accumulation and depletion in space. The vertical dashed line in the DOS shows the VBM. Adapted with permission from ref. 247 Copyright (2018) American Chemical Society.

 

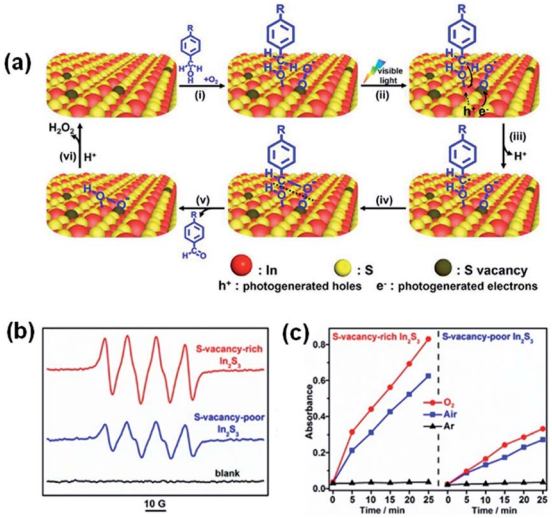


Fig. 17 (a) Proposed mechanism of the photooxidation of benzyl alcohol to benzaldehyde. (b) ESR spectra of SV-rich and SV-poor $In_2S_3$ in the presence of DMPO. (c) The dramatically different oxidation rates of the indicator molecule 3,3′,5,5′-tetramethylbenzidine in various gas environments (oxygen, air, and nitrogen) indicate that the ROS evolved from $O_2$. Adapted with permission from ref. 147 Copyright (2019) American Chemical Society.

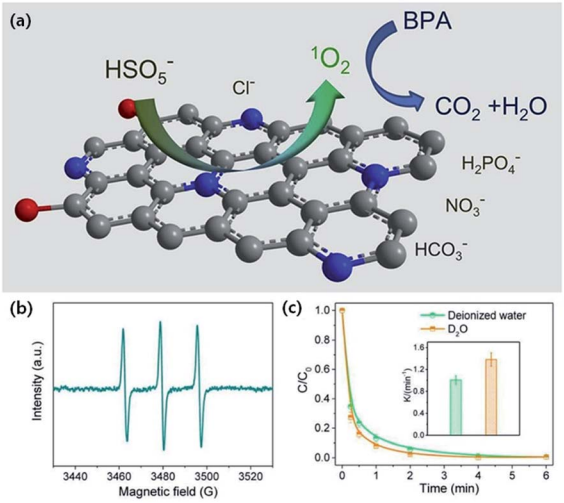


Fig. 18 (a) Schematic illustration of BPA degradation. (b) EPR spectrum of PMS activation. (c) Effect of $D_2O$ on BPA removal efficiency. Adapted with permission from ref. 275 Copyright (2019) Elsevier.

Enhanced generation of $O_2^{\bullet-}$ for selective photooxidation can also be accomplished on the defective surface with SVs. Sun *et al.* carried out a photocatalytic selective oxidation to convert alcohols to aldehydes with high efficiency and selectivity using defective $In_2S_3$ nanosheets (Fig. 17a and b).[147] The SVs-rich-$In_2S_3$ activates $O_2$ into $O_2^{\bullet-}$ *via* electron transfer, and the aldehyde selectivity is ≥98% for all alcohol substrates when SVs-rich $In_2S_3$ is used. For the oxidation of benzyl alcohol, the conversion rate of the substrate under ambient conditions is only 30% with SVs-poor $In_2S_3$ but 71% with SVs-rich $In_2S_3$ (Fig. 17c).

The selective oxidation of primary amines to imines is essential to synthesize dyes, fragrances, fungicides, pharmaceuticals, and agrochemicals.[265–268] Imines are normally synthesized in industry by the direct oxidation of amines or by the condensation of amines with aldehydes, which can require using stoichiometric amounts of harmful or hazardous reagents. Khampuanbut *et al.* utilized a $WO_3$/BiOBr photocatalyst for oxidizing amines to imine, for which $O_2^{\bullet-}$ is the main ROS and the OVs on $WO_3$/BiOBr promote the interfacial charge transfer.[269] Carrying out the reaction at room temperature under an $O_2$ atmosphere with visible light irradiation converts nearly 74.1% amines into imines within 4 h. Shi *et al.* used the phenol–$TiO_2$ complex as an efficient photocatalyst for the selective oxidation of amines to imines with the aid of $O_2$ under visible light irradiation.[270] Both primary and secondary amines can be oxidized to imines at >80% conversion rate in 30 min, and $O_2^{\bullet-}$ again proves to be the main ROS.

### 5.3 Singlet oxygen

**5.3.1 Scavenging pollutants.** Singlet oxygen is about 94 kJ $mol^{-1}$ more energetic than the ground state $O_2$ and has a mild redox potential ($E_0$ = 2.2 V *vs.* NHE). Herzberg first defined $^1O_2$ as the singlet oxygen in the excited state, but the importance of $^1O_2$ remained overlooked until 1964 when scientists showcased its use in chemical oxidation.[271,272] Although $^1O_2$ is not as strong as HO$^\bullet$ for the depletion of wastewater COD or TOC, the AOP based on $^1O_2$ generally use smaller amounts of oxidants and are less susceptible to radical scavengers.[158,273,274] Luo *et al.* used scavenger experiments and EPR analyses to prove that $^1O_2$ is the primary ROS for the degradation of organic matter such as BPA (Fig. 18).[275] Zhu *et al.* activated persulfate on β-$MnO_2$ nanorods to degrade phenol and verified that the ROS responsible for the oxidation is $^1O_2$ instead of $O_2^{\bullet-}$.[169] Liu *et al.* found that $^1O_2$ is the main ROS for the degradation of phenol over a wide pH range (pH = 3.5–9) in the CPANI-9/PMS system.[276] Sun *et al.* activated PDS with $FeCO_3$ and found that among the generated ROS ($^1O_2$, $SO_4^{\bullet-}$, and HO$^\bullet$), $^1O_2$ is key to the initial degradation rate of sulfadiazine and it contributes more to the oxidation reaction at higher pH.[277]

Zhao *et al.* showed that $^1O_2$ plays a dominant role in the removal of BPA catalyzed by deficient $ZnCoO_x$.[278] Bu *et al.* reported the OVs-mediated activation of PDS with BiOBr to degrade BPA, for which $^1O_2$ is the main ROS under alkaline conditions.[168] The removal ratio of TOC reaches 57.3% after 15 min in the reaction system (pH = 11.5), suggesting that BPA can be effectively mineralized into $CO_2$ and $H_2O$ by $^1O_2$. Li *et al.* developed $La_{1.15}FeO_3$ with rich surface OVs.[279] The catalyst has a high Fenton activity (0.0402 $min^{-1}$) for activating $H_2O_2$ to oxidize methyl orange, and the $^1O_2$ formed at the surface OVs is the main ROS. Gao *et al.* found that the piperazinyl, oxazinyl, and carboxylic substituents of ofloxacin are readily attacked by the $^1O_2$ generated from PMS with perovskites.[167] Both the amount of OVs of the perovskites and the degradation efficiency of ofloxacin fall in the order of $LaFeO_3$ < $LaZnO_3$ < $LaMnO_3$ < $LaNiO_3$.

**5.3.2 Generating value-added chemicals.** Many studies use $^1O_2$ as an environmentally benign, versatile, and moderate ROS

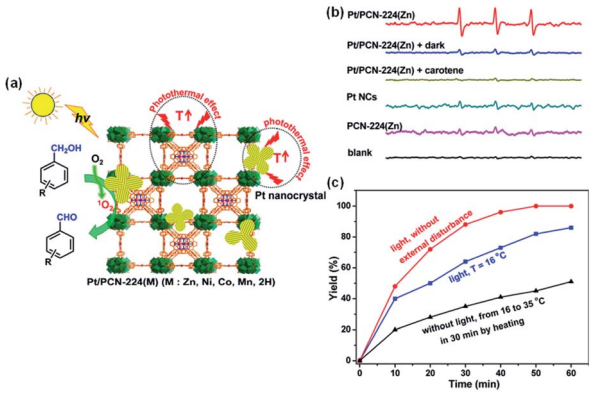


Fig. 19 (a) Schematic illustration showing the singlet oxygen-engaged selective oxidation of alcohols over Pt/PCN-224(M) using molecular oxygen under visible-light irradiation. (b) ESR spectra of the samples after mixing 4-oxo-TMP with PCN-224(Zn), Pt NCs, and Pt/PCN-224(Zn) in the absence or presence of carotene under visible-light irradiation or in the dark. (c) Oxidation yield of benzyl alcohol *vs.* the reaction time over Pt/PCN-224(Zn) in the presence or absence of light irradiation or external heating with other reaction parameters remaining identical. Adapted with permission from ref. 280 Copyright (2017) American Chemical Society.

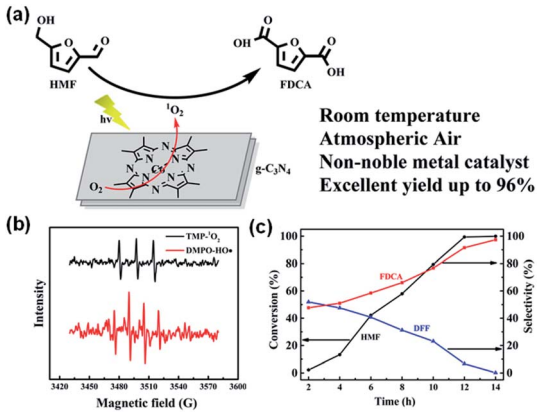


Fig. 20 (a) Possible mechanism of the photocatalytic oxidation of HMF with the CoPz/g-$C_3N_4$ catalyst. (b) EPR signals of the DMPO-HO$^{\bullet}$ adduct in water in the presence of bulk g-$C_3N_4$ and the TMP-$^1O_2$ adduct in water in the presence of CoPz/g-$C_3N_4$ in the photocatalysis process. (c) Photocatalytic performance. Adapted with permission from ref. 287 Copyright (2017) American Chemical Society.

for the selective oxidation of organic substances,[169,280] as $^1O_2$ shows high affinity for organic substrates with electron-rich moieties (*e.g.*, olefins, sulfides, and amines).[281,282]

Chen *et al.* developed a metal–organic framework based on Pt nanocrystals and porphyrin, denoted as Pt/PCN-224(M), to selectively oxidize aromatic alcohols to the corresponding aldehydes with $O_2$ (Fig. 19a).[280] Benzyl alcohol is oxidized with 1 atm $O_2$ at ambient temperature (16 °C) in water under visible light irradiation and the reaction is complete within 50 min. The 100% aldehyde selectivity can be attributed to $^1O_2$ as the main ROS, and extending the reaction time does not produce benzoic acid (Fig. 19b and c). Li *et al.* demonstrated the enhanced photocatalytic generation of $^1O_2$ with Mn–NCs@$SiO_2$–Pt and the selective oxidation of primary benzylic alcohols to aldehydes.[283] The energy transfer between the Mn-doped nanocrystals and molecular oxygen is made efficient thanks to the long half-life of the Mn excited state (in the order of milliseconds). Selective oxidization of glycerol to dihydroxyacetone (DHA) is a high-revenue chemical that has wide range of applications, *e.g.*, as a sun tanning agent in the cosmetics industry and as a precursor of pharmaceuticals or a building block for fine chemical synthesis, and can combine with lactic acid for producing biodegradable polymers.[284] Zhao *et al.* developed the Bi/$Bi_{3.64}Mo_{0.36}O_{6.55}$ heterostructure for the photocatalytic selective oxidization of glycerol.[285] The presence of OVs in Bi/$Bi_{3.64}Mo_{0.36}O_{6.55}$ promotes the mass production of $^1O_2$ as the ROS for the selective oxidation, and glycerol is oxidized in water to 1,3-dihydroxyacetone at ambient temperature (25 °C) with high selectivity (97–99%). Selective oxidation of organic sulfides has also sparked increasing attention as the resultant sulfoxides are key intermediates for the synthesis of agrochemicals, and pharmaceuticals as well as other valuable fine chemicals.[286] Wang *et al.* demonstrated the highly efficient and selective photo-oxidation of phenyl methyl sulfide to phenyl methyl sulfoxide catalyzed by OVs-$Bi_2O_3$.[158] The OVs in OVs-$Bi_2O_3$ can activate $O_2$ into $^1O_2$ in the dark, and the generation of $^1O_2$ is accelerated over both OVs-$Bi_2O_3$ and $Bi_2O_3$ when there is light irradiation. OVs-$Bi_2O_3$ has a stronger capability for the selective oxidation of phenyl methyl sulfide to phenyl methyl sulfoxide owing to its higher $^1O_2$ generation rate.

In addition, the $^1O_2$-mediated oxidation of HMF, a key biomass-derived intermediate, can give value-added products such as 2,5-furandicarboxylic acid (FDCA), which is an important monomer substitute for petrochemically-derived terephthalic acid to make polyethylene furanoate and other polymers (Fig. 20a).[287,288] Current technology for the oxidation of HMF to FDCA is costly as it normally needs to be run with noble metal catalysts at elevated temperatures (80–150 °C), thus needing high energy consumption and high oxygen pressure.[289] Xu *et al.* created a photocatalyst of cobalt thioporphyrazine (CoPz) dispersed on g-$C_3N_4$ for the oxidation of HMF to FDCA under simulated sunlight (Fig. 20b and c).[287] The reaction is performed at ambient temperature and air pressure, and the FDCA yield is 96.1%.

## 5.4 Surface lattice oxygen

**5.4.1 Scavenging pollutants.** Earth-abundant TMO have been used as good catalysts for environmental remediation applications. The oxidation capacity of OL is weak at a relatively low temperature (<200 °C), and $O_L$-mediated oxidations are generally carried out at elevated temperatures and a high partial pressure of oxygen.

Catalytic oxidation is the most appealing pathway to process effluent streams with dilute VOC (<0.5 vol%).[290,291] Conventional catalysts required for the oxidation of HCHO[292] normally contain noble metals (*e.g.*, Pt, Au, Pd, and Ag) that are costly and poorly available, and cheap and thermally stable TMO catalysts are excellent alternatives although their efficiency may be

 

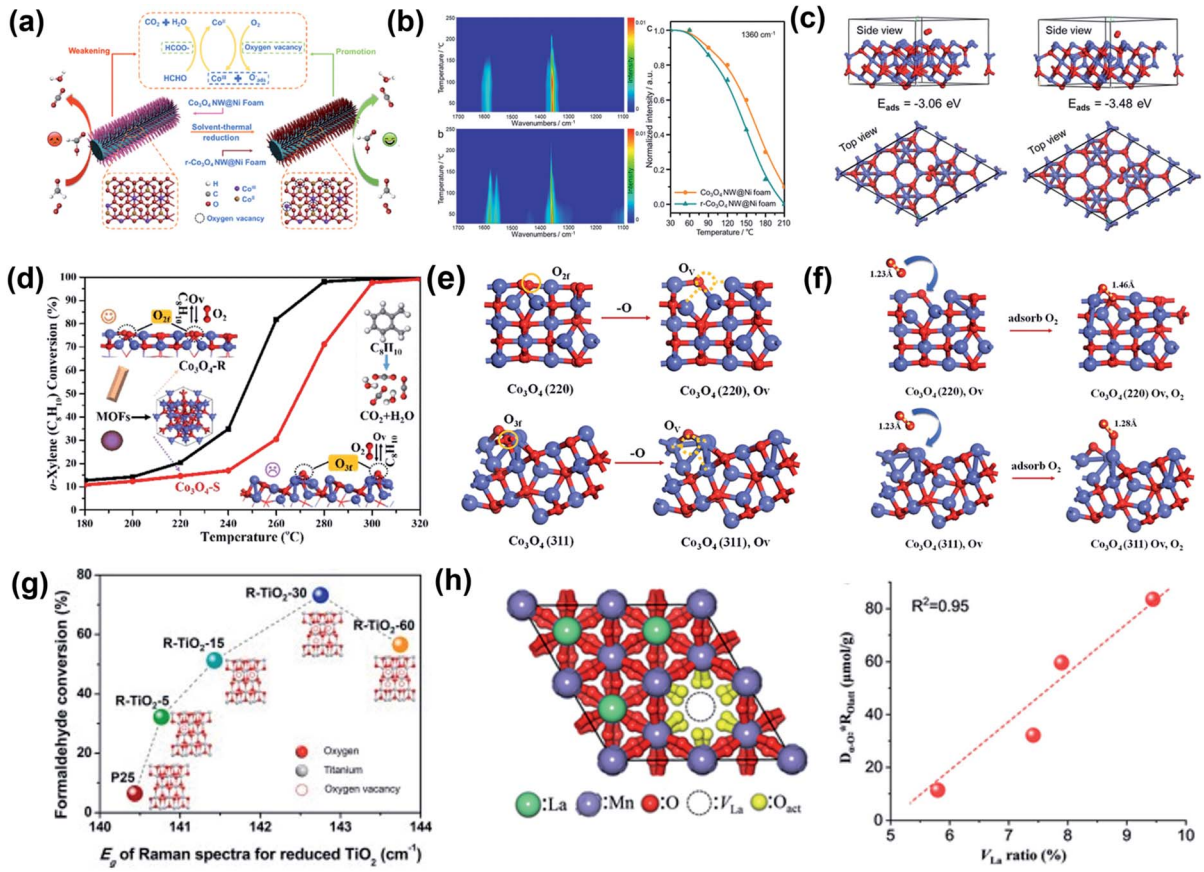


Fig. 21 (a) Schematic illustration of the catalytic oxidation of HCHO over r-$Co_3O_4$ NW@Ni with OVs; (b) *In situ* DRIFTs after HCHO adsorption over $Co_3O_4$ NW@Ni and r-$Co_3O_4$ NW@Ni catalysts as a function of temperature. (c) $O_2$ molecule adsorbed on the {111} surface of $Co_3O_4$ NW@Ni foam and r-$Co_3O_4$ NW@Ni catalysts. Adapted with permission from ref. 293 Copyright (2020) American Chemical Society. (d) Catalytic oxidation activities of *o*-xylene over MOF-derived $Co_3O_4$ with different shapes. (e) OV formation over the (220) and (311) surfaces of $Co_3O_4$, respectively; (f) side view of the adsorption configuration of $O_2$ over the (220) and (311) surfaces of $Co_3O_4$ with OVs. The Co and O atoms are in blue and red, respectively. Adapted with permission from ref. 294 Copyright (2021) American Chemical Society. (g) Formaldehyde conversion over reduced $TiO_2$ of different OV concentrations. Adapted with permission from ref. 296 Copyright (2019) Elsevier. (h) Activation of surface lattice oxygen induced by La vacancies and the amount of released surface $O_{latt}$ ($D\alpha$-$O_2$ $RO_{latt}$) as a function of $V_{La}$ ratio. Adapted with permission from ref. 297 Copyright (2021) Wiley-VCH Verlag GmbH & Co. KGaA.

somewhat lower. Zha *et al.* synthesized $Co_3O_4$ nanowires with abundant OVs grown *in situ* on the Ni foam (denoted as r-$Co_3O_4$ NW@Ni foam) as a stable catalyst for the highly efficient oxidation of HCHO to formate (Fig. 21a), and used the OVs-free $Co_3O_4$ NW@Ni foam and $Co_3O_4$ nanoparticles ($Co_3O_4$ NPs) to compare and characterize the catalytic performance.[293] The $T_{10\%}$ (*i.e.*, temperature at which HCHO conversion reaches 10%) of the catalysts ranks as r-$Co_3O_4$ NW@Ni foam (75 °C) < $Co_3O_4$ NW@Ni foam (100 °C) < $Co_3O_4$ NP (132 °C). According to *in situ* DRIFTs studies, HCHO and formate are slightly more easily adsorbed and formed on the OVs-free $Co_3O_4$ NW@Ni foam without $O_2$, but the formate species are more active on the surface of the r-$Co_3O_4$ NW@Ni foam (Fig. 21b). Further theoretical studies reveal that the abundant surface OVs reduce the adsorption energy of $O_2$, and r-$Co_3O_4$ NW@Ni can thus store more ROS and have a higher catalytic activity in HCHO oxidation (Fig. 21c). In another example, Ma *et al.* used MOF-derived $Co_3O_4$ with different shapes for the catalytic oxidation of *o*-xylene and studied how the surface twofold-coordinate lattice oxygen (O2f) creates higher catalyst reactivity (Fig. 21d).[294] The rod-like $Co_3O_4$-R has a lower $T_{90\%}$ (*i.e.*, temperature at which *o*-xylene conversion reaches at 90%) of 270 °C than the spherical $Co_3O_4$–S (about 290 °C). According to the OV formation energy and the adsorption energy of $O_2$, OVs are more easily formed and $O_2$ is more easily replenished on the $Co_3O_4$-R surface (Fig. 21e and f).

Wang *et al.* performed catalytic HCHO oxidation with three kinds of $Co_3O_4$ with different OV concentrations and demonstrated the dependence of the $O_L$ reactivity on the OV concentration.[295] The reaction rate constant ($k$) is 0.14 $min^{-1}$ for the $Co_3O_4$ nanobelts with a high OV concentration, which is about 20 times that of $Co_3O_4$ nanoplates (0.0071 $min^{-1}$). However, excessive OVs may also impair reactivity. For example, He *et al.* found that the catalytic activity of reduced $TiO_2$ for HCHO oxidation ranks as R-$TiO_2$-30 > R-$TiO_2$-60 > R-$TiO_2$-15 > R-$TiO_2$-5 (Fig. 21g).[296] In the catalytic reaction, $O_2$ is adsorbed on the surface of the reduced $TiO_2$, accepts electrons, and is transformed into active $O_L$ to degrade HCHO. However, excessive

OVs can reduce the adsorbed $O_2$ and trap electrons, and the formation of ROS from $O_2$ then becomes less effective.

Dong *et al.* developed a $CoMn_2O_4$ catalyst that has a lower activation energy (35.5 kJ $mol^{-1}$) for the oxidation of toluene than other metal oxides ($Co_3O_4$, $MnO_x$, and $Co_3O_4/MnO_x$).[293] The obtained $CoMn_2O_4$ has a large surface area, rich cationic vacancy, and high mobility of oxygen species, all of which contribute to the high catalytic activity. According to *in situ* temperature-programmed experiments, the surface $O_L$ induces the catalytic reaction, then gaseous $O_2$ is moved to the bulk phase lattice, and finally the bulk oxygen species is migrated to the surface to form more surface $O_L$ species at 200–250 °C. Toluene oxidation occurs *via* the benzyl alcohol-benzoate-anhydride-acetate reaction pathway over spinel $CoMn_2O_4$, and the conversion of the surface anhydride is the rate-determining step, especially at 200–210 °C.

For perovskites of the $ABO_3$ general formula, modulation of A-site defects can create effective oxidation catalysts that can be used in clean air applications. Liu *et al.* regulated the La vacancies ($V_{La}$) in $LaMnO_{3.15}$ by simply introducing urea in the traditional citrate-based synthesis to examine the relationship between the creation of $V_{La}$ and the activation of surface $O_L$ (Fig. 21h).[297] The $LaMnO_{3.15}$ catalyst with optimized $V_{La}$ achieves toluene oxidation at above 220 °C which is 10–25 times faster than the $LaMnO_{3.15}$ prepared from the traditional urea-free citric acid sol–gel method. The easier charge transfer from Mn to O in the $MnO_6$ octahedron activates the surface $O_L$ and enhances the redox properties of the $LaMnO_{3.15}$ perovskite, thus enabling superior performance.

**5.4.2 Generating value-added chemicals.** Chemists have long desired eliminating the use of oxidizing reagents that are expensive, toxic, or harmful in synthesis.[298] In this regard, the $O_L$ of oxides can serve as a mild oxidant to access specific products. For example, $O_L$ is readily used in the oxidation of alcohols to aldehydes ($RCH_2OH \rightarrow RCHO$). The selective oxidation of alcohols to aldehydes, one of the most fundamental oxidation reactions in organic synthesis for making drugs, fine chemicals, perfume, *etc.*, can be complicated by the formation of the corresponding acids or esters. Sabaté *et al.* found that Ru-doped $KMn_8O_{16}$ can efficiently catalyze the selective oxidation of alcohols to aldehydes with nearly 100% selectivity.[299] Dong *et al.* designed a $CeO_2$ decorated Au/CNT to catalyze the aerobic oxidization of benzyl alcohol.[300] The reaction gives benzaldehyde in 77.9% yield in 3 h under atmospheric pressure at 40 °C with 40 mL $min^{-1}$ $O_2$, and the $O_L$ of $CeO_2$ is the ROS for the reaction. Dai *et al.* reported that the $Bi_{24}O_{31}Br_{10}(OH)_\delta$ photocatalyst with active $O_L$ can selectively oxidize primary alcohols to aldehydes under visible light irradiation at room temperature using air.[301] The XPS analysis of the O1s spectra reveals that $O_L$ is converted to the adsorbed water on the catalyst surface after the reaction. With the developed catalyst, (1) aromatic alcohols are oxidized considerably faster than aliphatic alcohols, (2) benzyl alcohols with different functional groups (*e.g.*, *p*-$NO_2$, *p*-F, *p*-Cl, *p*-$CH_3$, *p*-$OCH_3$) are fully air-oxidized to the corresponding aldehydes with ≥99% selectivity within 4 h of illumination, and (3) there is no over-oxidation to carboxylic acids, CO, or $CO_2$ in all cases. Note that aldehydes are normally afforded from activated alcohols in which the carbon bears a phenyl group, such as benzyl alcohol,[302,303] probably because the electron-rich conjugated aromatic rings may lead to stronger adsorption on the catalyst surface.[304]

Conversely, $O_L$ is also used in various cases for the thorough oxidation of alcohols to carboxylic acids ($RCH_2OH \rightarrow RCOOH$). The aerobic oxidation of biomass to carboxylic acids under mild conditions is environmentally and economically advantageous to generate value-added chemicals from renewable feedstocks. Jin *et al.* found that Co-doped $Mg_3Al(OH)_y(CO_3)_z$ can promote the aerobic oxidation of glycerol into tartronic acid,[305] which is a high value-added chemical that has been widely used as a pharmaceutical and anti-corrosive protective agent, as well as for the monomer of biopolymers.[306] The complete conversion of glycerol is achieved with 64% selectivity of tartronic acid under mild conditions (70 °C, 0.1 MPa $O_2$). Hayashi *et al.* used $MnO_2$ for the aerobic oxidation of HMF and obtained FDCA in 95% yield under mild conditions (3 eq. $NaHCO_3$, 10 bar $O_2$, 120 °C, 24 h).[307] Han *et al.* prepared a mixed oxide $MnO_x$-$CeO_2$ (Mn/Ce = 6) catalyst *via* co-precipitation for the aerobic oxidation of HMF.[308] After 15 h at 110 °C in the presence of $KHCO_3$, the catalyst gives 91% FDCA yield and 98% HMF conversion. Zhang *et al.* prepared a series of Mn–Co binary oxides for the catalytic oxidation of HMF to FDCA and found that the $MnCo_2O_4$ catalyst is significantly better than $Mn_3O_4$, $Co_3O_4$, and other Mn–Co binary oxides with different Mn/Co molar ratios.[309] The $MnCo_2O_4$ catalyst has a Mn/Co molar ratio of 0.5, and gives 99.5% HMF conversion and 70.9% FDCA yield when the reaction is carried out at 100 °C under 10 bar $O_2$ with $KHCO_3$ for 24 h.

Reducing the OV formation energy increases the $O_L$ reactivity. Hayashi *et al.* found that compared with α- and γ-$MnO_2$, β- and λ-$MnO_2$ have lower OV formation energies due to their distinct crystal structures, and the OV formation energies of α- and γ-$MnO_2$ are higher both at the planar oxygen sites and at the bent oxygen sites.[172] The initial reaction rate per surface area of the catalysts for the aerobic oxidation of HMF to FDCA decreases in the order of β-$MnO_2$ (16.4 μmol $h^{-1}$ $m^{-2}$) > λ-$MnO_2$ (12.2 μmol $h^{-1}$ $m^{-2}$) > α-$MnO_2$ (7.6 μmol $h^{-1}$ $m^{-2}$) ≈ γ-$MnO_2$ (7.4 μmol $h^{-1}$ $m^{-2}$) > δ-$MnO_2$ (5.3 μmol $h^{-1}$ $m^{-2}$), which agrees well with what is expected from computational results. Wan *et al.* found that the high OV concentration of $CuMn_2O_4$ promotes the mobility and adsorption of oxygen species in the oxidation of HMF to FDCA.[310] Liu *et al.* demonstrated with DFT calculations that an increasing OV concentration boosts the $O_L$ reactivity of manganese oxide by reducing the OV formation energy, and also strengthens the adsorption and activation of $O_2$ to regenerate $O_L$ by significantly cutting down the $O_2$ adsorption energy, ultimately increasing the catalytic activity for the oxidation of HMF.[184]

Regulating the coordination environment of the metal also affects the activity of $O_L$. The coordination structures affect the M–O bond strength, and thu results in different mobilities of the lattice oxygen. From the Rietveld refinement of the X-ray diffractogram, Sabaté *et al.* determined that the interplanar spacing of the (100) plane of pristine $KMn_8O_{16}$ increased from

 

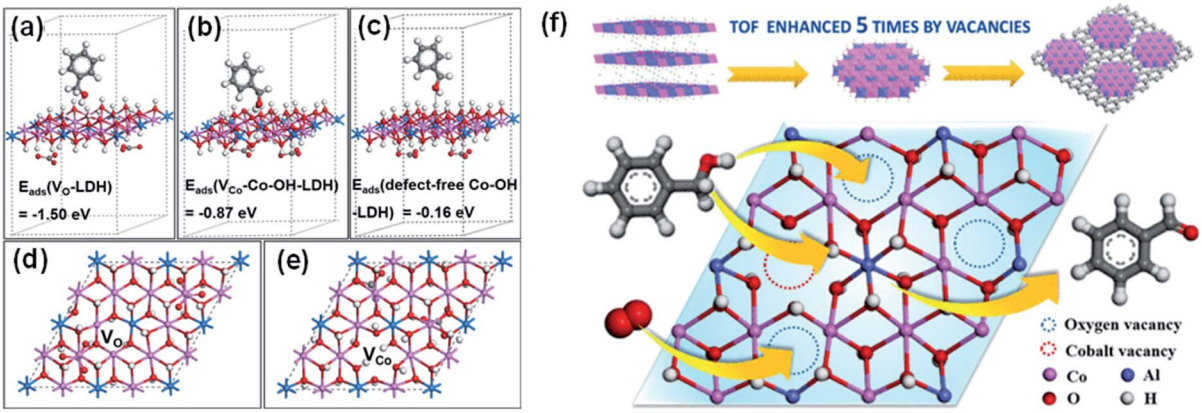


Fig. 22 DFT-calculated conformation of adsorption states and adsorption energies of a benzyl alcohol molecule on (a) an OV, (b) a $V_{Co}$–Co–$OH^{\delta-}$ site, and (c) defect-free Co–OH. Top views of the optimized structures of (d) an OV and (e) a Co vacancy. (f) Schematic diagram of Co-containing LDH for the aerobic oxidation of alcohols. Reproduced with permission. Adapted with permission from ref. 182 Copyright (2018) American Chemical Society.



7.1 to 7.7 Å after doping with Ru.[299,311] With the lattice expansion and the elongation of the Mn–O bond, the Ru-doped $KMn_8O_{16}$ can more easily lose its $O_L$ on the surface, thus allowing selective oxidation of alcohols to aldehydes.

Ishikawa *et al.* oxidized acrolein to acrylic acid with up to 98% selectivity by using orthorhombic Mo–V–Cu oxide as the catalyst.[312] The location of Cu under the oxygen defect site moderates the oxygen activation and prevents side reactions such as C–C scission to form $CO_x$ and acetic acid, thus improving the selectivity for acrylic acid.[313] The dispersion of noble metals (Au, Pt, Pd, Ru and Ag) can also regulate the coordination environment of TMO and generate $O_L$ with high reactivity thanks to the enhanced electronic metal-support interactions. Li *et al.* reported that the $O_L$ activated at the interfacial sites in $Au_1/CeO_2$ has lower OV formation energy (0.36 eV) and is more selective in oxidizing the alcohol substrate compared with the $O_L$ in Au NPs/$CeO_2$.[314]

Various studies have demonstrated reactions in which $O_L$ is the ROS directly responsible for the oxidation, and the OVs on the catalyst surface commonly expedite the dissociation of the O–H bond in the alcohol substrate.[315,316] Wang *et al.* used ultrathin CoAl-ELDH to catalyze the oxidation of benzyl alcohol to benzaldehyde.[182] The adsorption of benzyl alcohol is spontaneous and exothermic on the catalyst surface. The main active sites are OVs and $V_{Co}$–Co–$OH^{\delta-}$, where alcohol can be captured through linkage *via* its –OH group and the –OH group can then be activated and oxidized by the $O_L$ (Fig. 22). Dai *et al.* found that the $O_L$-mediated selective photo-oxidation of alcohols over $Bi_{24}O_{31}Br_{10}(OH)_\delta$ starts with the photo-dehydrogenation of alcohols to form adsorbed hydrogen species on the surface of the photocatalyst.[301] The $O_L$ of $Bi_{24}O_{31}Br_{10}(OH)_\delta$ then oxidizes the alcohol to form aldehydes and OVs, and the OVs are subsequently healed by mild oxidants ($O_2$ or benzoquinone) to complete the photocatalytic cycle.

While both $^1O_2$ and $O_L$ allow selective oxidations, oxidations mediated by $O_L$ are typically carried out under conditions such as high temperature and high humidity. Catalysts may collapse or agglomerate to a certain extent in these harsh environments, which will decrease the specific surface area and the number of exposed active sites. As a result, it may not be possible to maintain high catalytic efficiency and the catalyst may become deactivated. In contrast, $^1O_2$-mediated AOP are more favorable for selective oxidations; its catalytic conditions are milder, thus avoiding the agglomeration, collapse, and thus the deactivation of catalysts.

## 6 Challenges and perspectives

Various knowledge gaps remain in developing novel AOP and exploring the controllable reactivity of ROS. For example, although defect engineering has proven fruitful in accessing ROS for the desired AOP, some routes are sluggish and give interfering reactive species that do not contribute to the intended chemical transformation. To accomplish the rational design of catalysts and reactions, more understanding is needed regarding how the ROS contribute to the AOP and affect the selectivity and reactivity. To this end, *in situ* characterization techniques (*e.g.*, Raman, FTIR, and EPR) may be helpful for the on-line detection of ROS, and monitoring the transition states of the ROS, as well as verifying the interactions of the ROS with the organic substrate and oxidation pathways.

Controversy still exists regarding how the structures of catalysts, particularly the ubiquitous point defects, participate in the AOP. While in many cases OVs engage directly as active defect sites to accelerate the catalytic reaction,[305] at times the intrinsic properties of the catalyst altered by OVs are no less important.[118] The selective generation of ROS toward the specified oxidation reaction is still a growing research area, and various questions remain to be answered. For example, given a certain TMO catalyst, what kind of selectivity should be expected? What is the mechanistic aspect that can account for differences in the catalyst's behavior? How do researchers exercise control in designing catalysts? More research is needed on how the surface structure of catalysts regulate the generation and reactivity of ROS for intended reactions.

## Conflicts of interest

There are no conflicts to declare.

## Acknowledgements

This work was supported primarily by the National Key Research and Development Program of China (2020YFA0710303) and the National Natural Science Foundation of China (No. U1905215, 51772053 and 52072076). We thank Jay Wang for suggestions in writing.

## Notes and references

1 C. Xu, E. Paone, D. Rodriguez-Padron, R. Luque and F. Mauriello, *Chem. Soc. Rev.*, 2020, **49**, 4273–4306.
2 H. Luo, J. Barrio, N. Sunny, A. Li, L. Steier, N. Shah, I. E. L. Stephens and M. M. Titirici, *Adv. Energy Mater.*, 2021, **11**, 2101180–2101231.
3 Q. Chen, D. Yang, L. Yu, X. Jing and Y. Chen, *Mater. Horiz.*, 2020, **7**, 317–337.
4 Y. Shang, X. Xu, B. Gao, S. Wang and X. Duan, *Chem. Soc. Rev.*, 2021, **50**, 5281–5322.
5 F. Franco, C. Rettenmaier, H. S. Jeon and B. R. Cuenya, *Chem. Soc. Rev.*, 2020, **49**, 6884–6946.
6 H. Dong, G. Wei, D. Yin and X. Guan, *J. Hazard. Mater.*, 2020, **384**, 121497.
7 L. Luo, T. Zhang, M. Wang, R. Yun and X. Xiang, *ChemSusChem*, 2020, **13**, 5173–5184.
8 S. Wu, P. Wang, J. Qin, Y. Pei and Y. Wang, *Adv. Funct. Mater.*, 2021, **31**, 2102160.
9 J. L. Wang, X. C. Dai, H. L. Wang, H. L. Liu, J. Rabeah, A. Brückner, F. Shi, M. Gong and X. J. Yang, *Nat. Commun.*, 2021, **12**, 6840.
10 N. Zhang, Y. Zou, L. Tao, W. Chen, L. Zhou, Z. Liu, B. Zhou, G. Huang, H. Lin and S. Wang, *Angew. Chem., Int. Ed.*, 2019, **58**, 15895–15903.
11 B. H. Ko, B. Hasa, H. Shin, Y. Zhao and F. Jiao, *J. Am. Chem. Soc.*, 2022, **144**, 1258–1266.
12 K. Wang, C. Han, Z. Shao, J. Qiu, S. Wang and S. Liu, *Adv. Funct. Mater.*, 2021, **31**, 2102089.
13 Z. Z. Yang, C. Zhang, G. M. Zeng, X. F. Tan, H. Wang, D. l. Huang, K. H. Yang, J. J. Wei, C. Ma and K. Nie, *J. Mater. Chem. A*, 2020, **8**, 4141–4173.
14 Q. Zhang, D. He, X. Li, W. Feng, C. Lyu and Y. Zhang, *J. Hazard. Mater.*, 2020, **384**, 121350.
15 R. Pelalak, Z. Heidari, R. Alizadeh, E. Ghareshabani, N. Nasseh, A. Marjani, A. B. Albadarin and S. Shirazian, *J. Hazard. Mater.*, 2021, **411**, 125074.
16 Y. Sun, R. Li, C. Song, H. Zhang, Y. Cheng, A. Nie, H. Li, D. D. Dionysiou, J. Qian and B. Pan, *Appl. Catal., B*, 2021, **298**, 120537.
17 D. Wang and D. Astruc, *Chem. Soc. Rev.*, 2017, **46**, 816–854.
18 J. Wang and S. Wang, *Chem. Eng. J.*, 2021, **411**, 128392.
19 S. O. Ganiyu, S. Sable and M. Gamal El Din, *Chem. Eng. J.*, 2022, **429**, 132492.
20 Y. Ding, L. Fu, X. Peng, M. Lei, C. Wang and J. Jiang, *Chem. Eng. J.*, 2022, **427**, 131776.
21 J. Ye, G. Zhuang, Y. Wen, J. Wei, J. Chen, Z. Zhuang and Y. Yu, *Chem. Eng. J.*, 2019, **372**, 260–268.
22 Y. Zhu, X. Liu, S. Jin, H. Chen, W. Lee, M. Liu and Y. Chen, *J. Mater. Chem. A*, 2019, **7**, 5875–5897.
23 S. Wu, G. Zhuang, J. Wei, Z. Zhuang and Y. Yu, *J. Mater. Chem. A*, 2018, **6**, 18234–18241.
24 J. Azadmanjiri, V. K. Srivastava, P. Kumar, J. Wang and A. Yu, *J. Mater. Chem. A*, 2018, **6**, 13509–13537.
25 C. Xie, D. Yan, W. Chen, Y. Zou, R. Chen, S. Zang, Y. Wang, X. Yao and S. Wang, *Mater. Today*, 2019, **31**, 47–68.
26 S. Guo, Y. Jiang, L. Li, X. Huang, Z. Zhuang and Y. Yu, *J. Mater. Chem. A*, 2018, **6**, 4167–4178.
27 G. Zhuang, Y. Chen, Z. Zhuang, Y. Yu and J. Yu, *Sci. China Mater.*, 2020, **63**, 2089–2118.
28 M. Ai, J. W. Zhang, Y. W. Wu, L. Pan, C. Shi and J. J. Zou, *Chem.–Asian J.*, 2020, **15**, 3599.
29 J. Miao, X. Duan, J. Li, J. Dai, B. Liu, S. Wang, W. Zhou and Z. Shao, *Chem. Eng. J.*, 2019, **355**, 721–730.
30 Q. Lin and Y. Deng, *Environ. Sci. Technol.*, 2021, **55**, 15010–15012.
31 L. Xiong and J. Tang, *Adv. Energy Mater.*, 2021, **11**, 2003216.
32 J. Hoigné and H. Bader, *Water Res.*, 1983, **17**, 185–194.
33 Y. Nosaka and A. Y. Nosaka, *Chem. Rev.*, 2017, **117**, 11302–11336.
34 W. D. Oh, Z. Dong and T. T. Lim, *Appl. Catal., B*, 2016, **194**, 169–201.
35 W. A. Pryor, *Annu. Rev. Phytopathol.*, 1986, **48**, 657–667.
36 E. Codorniu-Hernández and P. G. Kusalik, *J. Am. Chem. Soc.*, 2012, **134**, 532–538.
37 J. L. Wang and L. J. Xu, *Crit. Rev. Environ. Sci. Technol.*, 2012, **42**, 251–325.
38 S. Luo, Z. Wei, D. D. Dionysiou, R. Spinney, W. P. Hu, L. Chai, Z. Yang, T. Ye and R. Xiao, *Chem. Eng. J.*, 2017, **327**, 1056–1065.
39 L. Wojnarovits and E. Takacs, *Radiat. Phys. Chem.*, 2014, **96**, 120–134.
40 D. Minakata, K. Li, P. Westerhoff and J. Crittenden, *Environ. Sci. Technol.*, 2009, **43**, 6220–6227.
41 E. W. Neuman, *J. Chem. Phys.*, 1934, **2**, 31–33.
42 D. T. Sawyer and J. S. Valentine, *Acc. Chem. Res.*, 1981, **14**, 393–400.
43 Q. Yi, J. Ji, B. Shen, C. Dong, J. Liu, J. Zhang and M. Xing, *Environ. Sci. Technol.*, 2019, **53**, 9725–9733.
44 E. A. Mayeda and A. J. Bard, *J. Am. Chem. Soc.*, 1973, **95**, 6223–6226.
45 C. Marques, J. M. F. Ferreira, E. Andronescu, D. Ficai, M. Sonmez and A. Ficai, *Int. J. Nanomed.*, 2014, **9**, 2713–2725.
46 L. De Trizio and L. Manna, *Chem. Rev.*, 2016, **116**, 10852–10887.
47 S. Korshunov and A. Imlay James, *J. Bacteriol.*, 2006, **188**, 6326–6334.
48 J. Ma, Z. Wei, R. Spinney, D. D. Dionysiou and R. Xiao, *Environ. Sci.: Water Res. Technol.*, 2021, **7**, 1966–1970.

 

49 Y. Pan, H. Xu, M. Chen, K. Wu, Y. Zhang and D. Long, *ACS Catal.*, 2021, **11**, 5974–5983.
50 C. Pan, L. Fu, F. Lide, Y. Ding, C. Wang, J. Huang and S. Wang, *Chem. Eng. J.*, 2022, **431**, 133957.
51 B. Cai, J. F. Feng, Q. Y. Peng, H. F. Zhao, Y. C. Miao and H. Pan, *J. Hazard. Mater.*, 2020, **392**, 122279.
52 M. Q. Yang, N. Zhang and Y. J. Xu, *ACS Appl. Mater. Interfaces*, 2013, **5**, 1156–1164.
53 C. Zhang, F. R. F. Fan and A. J. Bard, *J. Am. Chem. Soc.*, 2009, **131**, 177–181.
54 X. Ma, X. Li, J. Zhou, Y. Wang and X. Lang, *Chem. Eng. J.*, 2021, **426**, 131418.
55 E. J. Nanni and D. T. Sawyer, *J. Am. Chem. Soc.*, 1980, **102**, 7591–7593.
56 R. Dietz, A. E. J. Forno, B. E. Larcombe and M. E. Peover, *J. Chem. Soc. B*, 1970, 816–820.
57 M. V. Merritt and D. T. Sawyer, *J. Org. Chem.*, 1970, **35**, 2157–2159.
58 J. Wang and S. Wang, *Chem. Eng. J.*, 2020, **401**, 126158.
59 J. S. Filippo, C. I. Chern and J. S. Valentine, *J. Org. Chem.*, 1976, **41**, 1077–1078.
60 A. A. Ghogare and A. Greer, *Chem. Rev.*, 2016, **116**, 9994–10034.
61 M. Hayyan, M. A. Hashim and I. M. AlNashef, *Chem. Rev.*, 2016, **116**, 3029–3085.
62 R. W. Redmond and I. E. Kochevar, *Photochem. Photobiol.*, 2006, **82**, 1178–1186.
63 L. Chen, S. Wang, Z. Yang, J. Qian and B. Pan, *Appl. Catal., B*, 2021, **292**, 120193.
64 J. Lin, Q. Dai, H. Zhao, H. Cao, T. Wang, G. Wang and C. Chen, *Environ. Sci. Technol.*, 2021, **55**, 8683–8690.
65 X. Liu, A. Mazel, S. Marschner, Z. Fu, M. Muth, F. Kirschhöfer, G. Brenner-Weiss, S. Bräse, S. Diring and F. Odobel, *ACS Appl. Mater. Interfaces*, 2021, **13**, 57768–57773.
66 R. Ma, N. Liu, T. T. Lin, T. Zhao, S. L. Huang and G. Y. Yang, *J. Mater. Chem. A*, 2020, **8**, 8548–8553.
67 N. Zeinali, I. Oluwoye, M. Altarawneh and B. Z. Dlugogorski, *Ecotoxicol. Environ. Saf.*, 2019, **184**, 109605.
68 T. Matsuura, N. Yoshimura, A. Nishinaga and I. Saito, *Tetrahedron*, 1972, **28**, 4933–4938.
69 Y. Liu, W. Shu, K. Chen, Z. Peng and W. Chen, *ACS Catal.*, 2012, **2**, 2557–2565.
70 Y. Li, C. Wang, H. Zheng, F. Wan, F. Yu, X. Zhang and Y. Liu, *Appl. Surf. Sci.*, 2017, **391**, 654–661.
71 W. Li, J. Shi, K. H. L. Zhang and J. L. MacManus-Driscoll, *Mater. Horiz.*, 2020, **7**, 2832–2859.
72 S. Huang, T. Ouyang, B. F. Zheng, M. Dan and Z. Q. Liu, *Angew. Chem., Int. Ed.*, 2021, **60**, 9546–9552.
73 Y. Li, J. Huang, T. Peng, J. Xu and X. Zhao, *ChemCatChem*, 2010, **2**, 1082–1087.
74 L. Ren, M. Mao, Y. Li, L. Lan, Z. Zhang and X. Zhao, *Appl. Catal., B*, 2016, **198**, 303–310.
75 S. Albonetti, F. Cavani and F. TrifirÒ, *Catal. Rev.*, 1996, **38**, 413–438.
76 H. Xu, N. Yan, Z. Qu, W. Liu, J. Mei, W. Huang and S. Zhao, *Environ. Sci. Technol.*, 2017, **51**, 8879–8892.
77 C. H. Chung, F. Y. Tu, T. A. Chiu, T. T. Wu and W. Y. Yu, *Chem. Lett.*, 2021, **50**, 856–865.
78 M. Konsolakis, *Appl. Catal., B*, 2016, **198**, 49–66.
79 H. Jin, X. Tian, Y. Nie, Z. Zhou, C. Yang, Y. Li and L. Lu, *Environ. Sci. Technol.*, 2017, **51**, 12699–12706.
80 W. Dai, J. Long, L. Yang, S. Zhang, Y. Xu, X. Luo, J. Zou and S. Luo, *J. Energy Chem.*, 2021, **61**, 281–289.
81 S. Guan, L. Wang, S. M. Xu, D. Yang, G. I. N. Waterhouse, X. Qu and S. Zhou, *Chem. Sci.*, 2019, **10**, 2336–2341.
82 Z. Jiang, F. Yang, G. Yang, L. Kong, M. O. Jones, T. Xiao and P. P. Edwards, *J. Photochem. Photobiol., A*, 2010, **212**, 8–13.
83 Y. Zhu, R. Zhu, Y. Xi, J. Zhu, G. Zhu and H. He, *Appl. Catal., B*, 2019, **255**, 117739.
84 C. M. Lousada, A. J. Johansson, T. Brinck and M. Jonsson, *J. Phys. Chem. C*, 2012, **116**, 9533–9543.
85 C. C. Lin, F. R. Smith, N. Ichikawa, T. Baba and M. Itow, *Int. J. Chem. Kinet.*, 1991, **23**, 971–987.
86 A. Hiroki and J. A. LaVerne, *J. Phys. Chem. B*, 2005, **109**, 3364–3370.
87 J. Lee, U. von Gunten and J. H. Kim, *Environ. Sci. Technol.*, 2020, **54**, 3064–3081.
88 R. L. Johnson, P. G. Tratnyek and R. O. B. Johnson, *Environ. Sci. Technol.*, 2008, **42**, 9350–9356.
89 J. Wang and S. Wang, *Chem. Eng. J.*, 2018, **334**, 1502–1517.
90 J. Zhu, S. Wang, H. Li, J. Qian, L. Lv and B. Pan, *Water Res.*, 2021, **202**, 117397.
91 W. Ren, L. Xiong, X. Yuan, Z. Yu, H. Zhang, X. Duan and S. Wang, *Environ. Sci. Technol.*, 2019, **53**, 14595–14603.
92 S. Cai, Q. Zhang, Z. Wang, S. Hua, D. Ding, T. Cai and R. Zhang, *Appl. Catal., B*, 2021, **291**, 120093.
93 J. Hu, H. Dong, J. Qu and Z. Qiang, *Water Res.*, 2017, **112**, 1–8.
94 M. M. Montemore, M. A. van Spronsen, R. J. Madix and C. M. Friend, *Chem. Rev.*, 2018, **118**, 2816–2862.
95 C. Zhang, Z. Huang, J. Lu, N. Luo and F. Wang, *J. Am. Chem. Soc.*, 2018, **140**, 2032–2035.
96 Z. Xie, J. Zhang, Y. Xiao, Y. Xie, W. Zhu, S. Yu, T. Hou, S. Liang and L. Wang, *Energy Environ. Sci.*, 2021, **4**, 444–450.
97 L. Wenqian, H. Xu, L. Boda, Z. Bin, L. Ting, H. Ying and M. Jun, *Appl. Catal., B*, 2021, **305**, 121019.
98 H. Zhang, G. P. Hatzis, C. E. Moore, D. A. Dickie, M. W. Bezpalko, B. M. Foxman and C. M. Thomas, *J. Am. Chem. Soc.*, 2019, **141**, 9516–9520.
99 Y. Yang, K. Hu, P. Zhang, P. Zhou, X. Duan, H. Sun and S. Wang, *Small*, 2021, **17**, 2100927.
100 Y. Li, H. Dong, L. Li, L. Tang, R. Tian, R. Li, J. Chen, Q. Xie, Z. Jin, J. Xiao, S. Xiao and G. Zeng, *Water Res.*, 2021, **192**, 116850.
101 X. Chu, Y. Qu, A. Zada, L. Bai, Z. Li, F. Yang, L. Zhao, G. Zhang, X. Sun, Z. D. Yang and L. Jing, *Adv. Sci.*, 2020, **7**, 2001543.
102 X. Feng, J. Xu, X. Xu, S. Zhang, J. Ma, X. Fang and X. Wang, *ACS Catal.*, 2021, **11**, 12112–12122.
103 Z. Guo, B. Liu, Q. Zhang, W. Deng, Y. Wang and Y. Yang, *Chem. Soc. Rev.*, 2014, **43**, 3480–3524.
104 H. Arandiyan, S. S. Mofarah, C. C. Sorrell, E. Doustkhah, B. Sajjadi, D. Hao, Y. Wang, H. Sun, B. J. Ni, M. Rezaei,

Z. Shao and T. Maschmeyer, *Chem. Soc. Rev.*, 2021, **50**, 10116–10211.
105 M. Xing, W. Xu, C. Dong, Y. Bai, J. Zeng, Y. Zhou, J. Zhang and Y. Yin, *Chem*, 2018, **4**, 1359–1372.
106 R. Yang, Y. Fan, R. Ye, Y. Tang, X. Cao, Z. Yin and Z. Zeng, *Adv. Mater.*, 2021, **33**, 2004862.
107 N. Thomas, D. D. Dionysiou and S. C. Pillai, *J. Hazard. Mater.*, 2021, **404**, 124082.
108 X. Wang, W. Liu, J. Qin and L. Lei, *Ind. Eng. Chem. Res.*, 2020, **59**, 2192–2202.
109 Q. Wu, H. Yang, L. Kang, Z. Gao and F. Ren, *Appl. Catal., B*, 2020, **263**, 118282.
110 W. Jiang, D. D. Dionysiou, M. Kong, Z. Liu, Q. Sui and S. Lyu, *Chem. Eng. J.*, 2020, **380**, 122537.
111 M. E. Lindsey and M. A. Tarr, *Environ. Sci. Technol.*, 2000, **34**, 444–449.
112 L. Lyu, L. Zhang, G. He, H. He and C. Hu, *J. Mater. Chem. A*, 2017, **5**, 7153–7164.
113 L. Z. Huang, M. Zhu, Z. Liu, Z. Wang and H. C. B. Hansen, *J. Hazard. Mater.*, 2019, **364**, 39–47.
114 J. Y. Qiu, J. H. Chen, B. Y. Xiao, X. X. Li, T. Wan, F. H. Qin, Y. Mi and Z. Y. Huang, *Catal. Lett.*, 2020, **150**, 222–233.
115 A. Y. Zhang, T. Lin, Y. Y. He and Y. X. Mou, *J. Hazard. Mater.*, 2016, **311**, 81–90.
116 B. Gong, C. Ku, H. Q. Yu and P. H. L. Sit, *J. Phys. Chem. C*, 2021, **125**, 8508–8517.
117 W. Liu, J. Tian, C. Mao, Z. Wang, J. Liu, R. A. Dahlgren, L. Zhang and X. Wang, *Anal. Chim. Acta*, 2020, **1127**, 246–255.
118 Z. Tan, J. Zhang, Y. C. Chen, J. P. Chou and Y. K. Peng, *J. Phys. Chem. Lett.*, 2020, **11**, 5390–5396.
119 S. Zhan, H. Zhang, X. Mi, Y. Zhao, C. Hu and L. Lyu, *Environ. Sci. Technol.*, 2020, **54**, 8333–8343.
120 Z. Weng, J. Li, Y. Weng, M. Feng, Z. Zhuang and Y. Yu, *J. Mater. Chem. A*, 2017, **5**, 15650–15660.
121 X. Zhang, T. Li, M. Guan, R. Li, J. Liu, Y. Wang, C. Zhang and C. Fan, *Appl. Surf. Sci.*, 2021, **567**, 150828.
122 M. Setvin, U. Aschauer, P. Scheiber, Y. F. Li, W. Hou, M. Schmid, A. Selloni and U. Diebold, *Science*, 2013, **341**, 988–991.
123 S. Zhao, Y. Wen, X. Liu, X. Pen, F. Lu, F. Gao, X. Xie, C. Du, H. Yi, D. Kang and X. Tang, *Nano Res.*, 2020, **13**, 1544–1551.
124 H. Y. Gao, C. H. Huang, L. Mao, B. Shao, J. Shao, Z. Y. Yan, M. Tang and B.-Z. Zhu, *Environ. Sci. Technol.*, 2020, **54**, 14046–14056.
125 D. E. Pennington and A. Haim, *J. Am. Chem. Soc.*, 1968, **90**, 3700–3704.
126 R. O. C. Norman, P. M. Storey and P. R. West, *J. Chem. Soc. B*, 1970, 1087–1095, DOI: 10.1039/J29700001087.
127 N. Chen, D. Lee, H. Kang, D. Cha, J. Lee and C. Lee, *J. Environ. Chem. Eng.*, 2022, **10**, 107654.
128 J. D. Rush and B. H. J. Bielski, *J. Phys. Chem.*, 1985, **89**, 5062–5066.
129 K. Xu and U. von Gunten, *ACS ES&T Engineering*, 2021, **1**, 1410–1419.
130 Z. Wu, K. Guo, S. Cao, W. Yao and L. Piao, *Nano Res.*, 2020, **13**, 551–556.
131 E. S. Kumar, S. Venkatesh and M. S. R. Rao, *Appl. Phys. Lett.*, 2010, **96**, 232504.
132 Z. Wei, D. Liu, W. Wei, X. Chen, Q. Han, W. Yao, X. Ma and Y. Zhu, *ACS Appl. Mater. Interfaces*, 2017, **9**, 15533–15540.
133 T. Mallat and A. Baiker, *Chem. Rev.*, 2004, **104**, 3037–3058.
134 T. Matsumoto, M. Ueno, N. Wang and S. Kobayashi, *Chem.–Asian J.*, 2008, **3**, 196–214.
135 B. Z. Zhan and A. Thompson, *Tetrahedron*, 2004, **60**, 2917–2935.
136 P. Lyu, J. Zhu, C. Han, L. Qiang, L. Zhang, B. Mei, J. He, X. Liu, Z. Bian and H. Li, *ACS Appl. Mater. Interfaces*, 2021, **13**, 2033–2043.
137 H. Shang, M. Li, H. Li, S. Huang, C. Mao, Z. Ai and L. Zhang, *Environ. Sci. Technol.*, 2019, **53**, 6444–6453.
138 W. Qin, G. Fang, Y. Wang and D. Zhou, *Chem. Eng. J.*, 2018, **348**, 526–534.
139 W. Li, X. He, B. Li, B. Zhang, T. Liu, Y. Hu and J. Ma, *Appl. Catal., B*, 2022, **305**, 121019.
140 H. Li, H. Zhu, Y. Shi, H. Shang, L. Zhang and J. Wang, *Environ. Sci. Technol.*, 2022, **56**, 1771–1779.
141 H. Li, F. Qin, Z. Yang, X. Cui, J. Wang and L. Zhang, *J. Am. Chem. Soc.*, 2017, **139**, 3513–3521.
142 J. Li, C. Shu, C. Liu, X. Chen, A. Hu and J. Long, *Small*, 2020, **16**, 2001812.
143 J. Wu, X. Li, W. Shi, P. Ling, Y. Sun, X. Jiao, S. Gao, L. Liang, J. Xu, W. Yan, C. Wang and Y. Xie, *Angew. Chem., Int. Ed.*, 2018, **57**, 8719–8723.
144 M. Kim, B. Lee, H. Ju, J. Y. Kim, J. Kim and S. W. Lee, *Adv. Mater.*, 2019, **31**, 1903316.
145 Y. Mao, P. Wang, L. Li, Z. Chen, H. Wang, Y. Li and S. Zhan, *Angew. Chem., Int. Ed.*, 2020, **59**, 3685–3690.
146 T. Gan, J. Yang, D. Morris, X. Chu, P. Zhang, W. Zhang, Y. Zou, W. Yan, S. H. Wei and G. Liu, *Nat. Commun.*, 2021, **12**, 2741.
147 X. Sun, X. Luo, X. Zhang, J. Xie, S. Jin, H. Wang, X. Zheng, X. Wu and Y. Xie, *J. Am. Chem. Soc.*, 2019, **141**, 3797–3801.
148 F. Rao, G. Zhu, W. Zhang, Y. Xu, B. Cao, X. Shi, J. Gao, Y. Huang, Y. Huang and M. Hojamberdiev, *ACS Catal.*, 2021, **11**, 7735–7749.
149 Y. Zhao and H. Wang, *Langmuir*, 2021, **37**, 13969–13975.
150 Y. Yin, R. Lv, X. Li, L. Lv and W. Zhang, *Appl. Catal., B*, 2021, **299**, 120685.
151 Z. Yang, J. Qian, A. Yu and B. Pan, *Proc. Natl. Acad. Sci. U. S. A.*, 2019, **116**, 6659–6664.
152 Y. Yin, Y. Ren, J. Lu, W. Zhang, C. Shan, M. Hua, L. Lv and B. Pan, *Appl. Catal., B*, 2021, **286**, 120282.
153 X. Li, J. Wang, X. Duan, Y. Li, X. Fan, G. Zhang, F. Zhang and W. Peng, *ACS Catal.*, 2021, **11**, 4848–4861.
154 B. F. Sels, D. E. De Vos and P. A. Jacobs, *J. Am. Chem. Soc.*, 2007, **129**, 6916–6926.
155 X. Li, J. Liu, A. I. Rykov, H. Han, C. Jin, X. Liu and J. Wang, *Appl. Catal., B*, 2015, **179**, 196–205.
156 S. Chong, G. Zhang, N. Zhang, Y. Liu, T. Huang and H. Chang, *J. Hazard. Mater.*, 2017, **334**, 150–159.
157 M. C. DeRosa and R. J. Crutchley, *Coord. Chem. Rev.*, 2002, **233–234**, 351–371.

 

158 J. Wang, X. Xu, Y. Liu, Z. Wang, P. Wang, Z. Zheng, H. Cheng, Y. Dai and B. Huang, *ChemSusChem*, 2020, **13**, 3488–3494.
159 J. Ji, Q. Yan, P. Yin, S. Mine, M. Matsuoka and M. Xing, *Angew. Chem., Int. Ed.*, 2021, **60**, 2903–2908.
160 W. J. Duan, J. L. He, Z. L. Wei, Z. R. Dai and C. H. Feng, *Environ. Sci.: Nano*, 2020, **7**, 2982–2994.
161 T. Liu, D. Zhang, K. Yin, C. Yang, S. Luo and J. C. Crittenden, *Chem. Eng. J.*, 2020, **388**, 124264.
162 Q. Ye, J. Wu, P. Wu, S. Rehman, Z. Ahmed and N. Zhu, *Chem. Eng. J.*, 2021, **417**, 12911.
163 L. Kong, G. Fang, Z. Fang, Y. Zou, F. Zhu, D. Zhou and J. Zhan, *Chem. Eng. J.*, 2021, **416**, 128996.
164 M. I. Akhtar, F. Junejo, H. I. Naqvi, M. Hamid, Y. Wang, M. Liu, C. Hu, Y. Xin, D. Ma, M. Gao and H. Xie, *Chem. Eng. J.*, 2022, **433**, 134048.
165 H. Zeng, L. Deng, H. Zhang, C. Zhou and Z. Shi, *J. Hazard. Mater.*, 2020, **400**, 123297.
166 Y. Zhao, H. An, G. Dong, J. Feng, T. Wei, Y. Ren and J. Ma, *Chem. Eng. J.*, 2020, **388**, 124371.
167 P. Gao, X. Tian, Y. Nie, C. Yang, Z. Zhou and Y. Wang, *Chem. Eng. J.*, 2019, **359**, 828–839.
168 Y. Bu, H. Li, W. Yu, Y. Pan, L. Li, Y. Wang, L. Pu, J. Ding, G. Gao and B. Pan, *Environ. Sci. Technol.*, 2021, **55**, 2110–2120.
169 S. Zhu, X. Li, J. Kang, X. Duan and S. Wang, *Environ. Sci. Technol.*, 2019, **53**, 307–315.
170 A. Jawad, K. Zhan, H. Wang, A. Shahzad, Z. Zeng, J. Wang, X. Zhou, H. Ullah, Z. Chen and Z. Chen, *Environ. Sci. Technol.*, 2020, **54**, 2476–2488.
171 J. Hu, X. Zeng, G. Wang, B. Qian, Y. Liu, X. Hu, B. He, L. Zhang and X. Zhang, *Chem. Eng. J.*, 2020, **400**, 125869.
172 E. Hayashi, Y. Yamaguchi, K. Kamata, N. Tsunoda, Y. Kumagai, F. Oba and M. Hara, *J. Am. Chem. Soc.*, 2019, **141**, 890–900.
173 H. Liu, W. Jia, X. Yu, X. Tang, X. Zeng, Y. Sun, T. Lei, H. Fang, T. Li and L. Lin, *ACS Catal.*, 2021, **11**, 7828–7844.
174 X. Xu, L. Li, J. Huang, H. Jin, X. Fang, W. Liu, N. Zhang, H. Wang and X. Wang, *ACS Catal.*, 2018, **8**, 8033–8045.
175 P. Schlexer, D. Widmann, R. J. Behm and G. Pacchioni, *ACS Catal.*, 2018, **8**, 6513–6525.
176 N. H. M. Dostagir, R. Rattanawan, M. Gao, J. Ota, J. Y. Hasegawa, K. Asakura, A. Fukouka and A. Shrotri, *ACS Catal.*, 2021, **11**, 9450–9461.
177 M. Zhao, J. Deng, J. Liu, Y. Li, J. Liu, Z. Duan, J. Xiong, Z. Zhao, Y. Wei, W. Song and Y. Sun, *ACS Catal.*, 2019, **9**, 7548–7567.
178 X. Zhang, C. Pei, X. Chang, S. Chen, R. Liu, Z. J. Zhao, R. Mu and J. Gong, *J. Am. Chem. Soc.*, 2020, **142**, 11540–11549.
179 X. Yang, X. Yu, M. Jing, W. Song, J. Liu and M. Ge, *ACS Appl. Mater. Interfaces*, 2019, **11**, 730–739.
180 A. D. Quinonero, E. B. Garcia, S. L. Rodriguez, J. Juan, D. L. Castello, M. G. Melchor, F. C. Herrera, E. Pellegrin, C. Escudero and A. B. Lopez, *ACS Catal.*, 2020, **10**, 6532–6545.
181 J. Lu, J. Wang, Q. Zou, D. He, L. Zhang, Z. Xu, S. He and Y. Luo, *ACS Catal.*, 2019, **9**, 2177–2195.
182 Q. Wang, L. Chen, S. Guan, X. Zhang, B. Wang, X. Cao, Z. Yu, Y. He, D. G. Evans, J. Feng and D. Li, *ACS Catal.*, 2018, **8**, 3104–3115.
183 Q. Gao, G. Wang, Y. Chen, B. Han, K. Xia and C. Zhou, *Environ. Sci.: Water Res. Technol.*, 2021, **7**, 1197–1211.
184 W. Sang, Z. Li, M. Huang, X. Wu, D. Li, L. Mei and J. Cui, *Chem. Eng. J.*, 2020, **383**, 123057.
185 S. Hussain, E. Aneggi and D. Goi, *Environ. Chem. Lett.*, 2021, **19**, 2405–2424.
186 F. Chen, X. L. Wu, C. Shi, H. Lin, J. Chen, Y. Shi, S. Wang and X. Duan, *Adv. Funct. Mater.*, 2021, **31**, 2007877.
187 G. P. Anipsitakis and D. D. Dionysiou, *Environ. Sci. Technol.*, 2004, **38**, 3705–3712.
188 X. Zhao, X. Li, Z. Zhu, W. Hu, H. Zhang, J. Xu, X. Hu, Y. Zhou, M. Xu, H. Zhang and G. Hu, *Appl. Catal., B*, 2022, **300**, 120759.
189 L. S. Zhang, X. H. Jiang, Z. A. Zhong, L. Tian, Q. Sun, Y. T. Cui, X. Lu, J. P. Zou and S. L. Luo, *Angew. Chem., Int. Ed.*, 2021, **60**, 21751–21755.
190 L. Wu, Z. Sun, Y. Zhen, S. Zhu, C. Yang, J. Lu, Y. Tian, D. Zhong and J. Ma, *Environ. Sci. Technol.*, 2021, **55**, 15400–15411.
191 H. Zhao, X. Liu, Y. Dong, Y. Xia and H. Wang, *Appl. Catal., B*, 2019, **256**, 117872.
192 C. Y. Toe, C. Tsounis, J. Zhang, H. Masood, D. Gunawan, J. Scott and R. Amal, *Environ. Sci. Technol.*, 2021, **14**, 1140–1175.
193 Z. Geng, X. Kong, W. Chen, H. Su, Y. Liu, F. Cai, G. Wang and J. Zeng, *Angew. Chem., Int. Ed.*, 2018, **57**, 6054–6059.
194 J. Xiang, T. Zhang, R. Cao, M. Lin, B. Yang, Y. Wen, Z. Zhuang and Y. Yu, *Sol. RRL*, 2021, **5**, 2100703.
195 M. Yang, T. Xu, X. Jin, Q. Shen and C. Sun, *Appl. Surf. Sci.*, 2022, **581**, 152439.
196 J. Sahu, S. Kumar, V. S. Vats, P. A. Alvi, B. Dalela, S. Kumar and S. Dalela, *J. Lumin.*, 2022, **243**, 118673.
197 Q. Wang, Z. Liu, D. Liu, W. Wang, Z. Zhao, F. Cui and G. Li, *Chem. Eng. J.*, 2019, **360**, 838–847.
198 M. J. Jackson, *Proc. Nutr. Soc.*, 1999, **58**, 1001–1006.
199 C. D. Jaeger and A. J. Bard, *J. Phys. Chem.*, 1979, **83**, 3146–3152.
200 K. Hiramoto, H. Johkoh, K. I. Sako and K. Kikugawa, *Free Radical Res. Commun.*, 1993, **19**, 323–332.
201 J. M. Burns, W. J. Cooper, J. L. Ferry, D. W. King, B. P. DiMento, K. McNeill, C. J. Miller, W. L. Miller, B. M. Peake, S. A. Rusak, A. L. Rose and T. D. Waite, *Aquat. Sci.*, 2012, **74**, 683–734.
202 Y. Jing and B. P. Chaplin, *Environ. Sci. Technol.*, 2017, **51**, 2355–2365.
203 C. C. Perry, V. J. Tang, K. M. Konigsfeld, J. A. Aguilera and J. R. Milligan, *J. Phys. Chem. B*, 2011, **115**, 9889–9897.
204 C. Yu, Y. Wu, F. Zeng and S. Wu, *J. Mater. Chem. B*, 2013, **1**, 4152–4159.
205 T. Charbouillot, M. Brigante, G. Mailhot, P. R. Maddigapu, C. Minero and D. Vione, *J. Photochem. Photobiol., A*, 2011, **222**, 70–76.

206 M. Náfrádi, L. Farkas, T. Alapi, K. Hernádi, K. Kovács, L. Wojnárovits and E. Takács, *Radiat. Phys. Chem.*, 2020, **170**, 108610.
207 C. He, Y. Wang, Z. Li, Y. Huang, Y. Liao, D. Xia and S. Lee, *Environ. Sci. Technol.*, 2020, **54**, 12771–12783.
208 T. Wu, T. Lin, J. Zhao, H. Hidaka and N. Serpone, *Environ. Sci. Technol.*, 1999, **33**, 1379–1387.
209 L. Liang, Q. Chang, T. Cai, N. Li, C. Xue, J. Yang and S. Hu, *Chem. Eng. J.*, 2022, **428**, 131139.
210 M. I. Muniz-Junqueira and V. N. de Paula-Coelho, *Int. Immunopharmacol.*, 2008, **8**, 1633–1638.
211 Y. Guo and B. Li, *Carbon*, 2015, **82**, 459–469.
212 Y. Kakuma, A. Y. Nosaka and Y. Nosaka, *Phys. Chem. Chem. Phys.*, 2015, **17**, 18691–18698.
213 K. K. Mothilal, J. Johnson Inbaraj, R. Gandhidasan and R. Murugesan, *J. Photochem. Photobiol., A*, 2004, **162**, 9–16.
214 R. Konaka, E. Kasahara, W. C. Dunlap, Y. Yamamoto, K. C. Chien and M. Inoue, *Free Radical Biol. Med.*, 1999, **27**, 294–300.
215 L. R. Barclay, M. C. Basque and M. R. Vinqvist, *Can. J. Chem.*, 2003, **81**, 457–467.
216 J. A. Rengifo-Herrera, K. Pierzchała, A. Sienkiewicz, L. Forró, J. Kiwi and C. Pulgarin, *Appl. Catal., B*, 2009, **88**, 398–406.
217 X. Ragàs, A. Jiménez-Banzo, D. Sánchez-García, X. Batllori and S. Nonell, *Chem. Commun.*, 2009, 2920–2922, DOI: 10.1039/B822776D.
218 A. M. Asadirad, Z. Erno and N. R. Branda, *Chem. Commun.*, 2013, **49**, 5639–5641.
219 H. Wang, X. Yang, W. Shao, S. Chen, J. Xie, X. Zhang, J. Wang and Y. Xie, *J. Am. Chem. Soc.*, 2015, **137**, 11376–11382.
220 M. Wozniak, F. Tanfani, E. Bertoli, G. Zolese and J. Antosiewicz, *Biochim. Biophys. Acta, Lipids Lipid Metab.*, 1991, **1082**, 94–100.
221 Z. C. Redman, J. Wesolowski and P. L. Tomco, *Environ. Sci. Technol.*, 2021, **55**, 4974–4983.
222 C. Liang, H. P. Feng, H. Y. Niu, C. G. Niu, J. S. Li, D. W. Huang, L. Zhang, H. Guo, N. Tang and H. Y. Liu, *Chem. Eng. J.*, 2020, **384**, 123236.
223 Z. Wang, J. Wang, B. Xiong, F. Bai, S. Wang, Y. Wan, L. Zhang, P. Xie and M. R. Wiesner, *Environ. Sci. Technol.*, 2020, **54**, 464–475.
224 S. Kang, L. Zhang, C. Yin, Y. Li, L. Cui and Y. Wang, *Appl. Catal., B*, 2017, **211**, 266–274.
225 P. Neta, V. Madhavan, H. Zemel and R. W. Fessenden, *J. Am. Chem. Soc.*, 1977, **99**, 163–164.
226 S. Gligorovski, R. Strekowski, S. Barbati and D. Vione, *Chem. Rev.*, 2015, **115**, 13051–13092.
227 K. Bao, S. Zhang, P. Ni, Z. Zhang, K. Zhang, L. Wang, L. X. Sun, W. Mao, Q. Zhou and Y. Qian, *Catal. Today*, 2020, **340**, 311–317.
228 L. Hu, Y. Liao, D. Xia, F. Peng, L. Tan, S. Hu, C. Zheng, X. Lu, C. He and D. Shu, *Chem. Eng. J.*, 2020, **385**, 123824.
229 H. Guo, C. G. Niu, C. Y. Feng, C. Liang, L. Zhang, X. J. Wen, Y. Yang, H. Y. Liu, L. Li and L. S. Lin, *Chem. Eng. J.*, 2020, **385**, 123919.
230 H. Xu, Q. Ye, J. Zhang, Q. Li, M. Wang, P. Zhou, G. Zhou and Q. Wang, *Sci. Total Environ.*, 2021, **778**, 146280.
231 Y. Liu, X. Liu, Y. Zhao and D. D. Dionysiou, *Appl. Catal., B*, 2017, **213**, 74–86.
232 A. A. Gorman and M. A. J. Rodgers, *Chem. Soc. Rev.*, 1981, **10**, 205–231.
233 X. Chen, W. D. Oh and T. T. Lim, *Chem. Eng. J.*, 2018, **354**, 941–976.
234 Z. Xiong, Y. Jiang, Z. Wu, G. Yao and B. Lai, *Chem. Eng. J.*, 2021, **421**, 127863.
235 M. Zhang, R. Luo, C. Wang, W. Zhang, X. Yan, X. Sun, L. Wang and J. Li, *J. Mater. Chem. A*, 2019, **7**, 12547–12555.
236 W. R. Haag and J. Hoigne, *Environ. Sci. Technol.*, 1986, **20**, 341–348.
237 M. A. Oturan and J. J. Aaron, *Crit. Rev. Environ. Sci. Technol.*, 2014, **44**, 2577–2641.
238 X. Ye, Y. Cui, X. Qiu and X. Wang, *Appl. Catal., B*, 2014, **152**, 383–389.
239 G. V. Buxton, C. L. Greenstock, W. P. Helman and A. B. Ross, *J. Phys. Chem. Ref. Data*, 1988, **17**, 513–886.
240 B. Ervens, S. Gligorovski and H. Herrmann, *Phys. Chem. Chem. Phys.*, 2003, **5**, 1811–1824.
241 X. X. Guo, T. T. Hu, B. Meng, Y. Sun and Y. F. Han, *Appl. Catal., B*, 2020, **260**, 118157.
242 N. Zhang, E. P. Tsang, J. Chen, Z. Fang and D. Zhao, *J. Colloid Interface Sci.*, 2020, **558**, 163–172.
243 H. Li, J. Shang, Z. Yang, W. Shen, Z. Ai and L. Zhang, *Environ. Sci. Technol.*, 2017, **51**, 5685–5694.
244 M. T. Bender, Y. C. Lam, S. Hammes-Schiffer and K. S. Choi, *J. Am. Chem. Soc.*, 2020, **142**, 21538–21547.
245 Z. Liu, Z. Zhao, W. Jiang, Z. Zhu, Y. Wang, Z. Liu, W. Gu, Y. Yang, Y. Yang, L. Zhang, W. Yao and F. Teng, *Appl. Catal., B*, 2021, **298**, 120517.
246 L. Luo, Z. J. Wang, X. Xiang, D. Yan and J. Ye, *ACS Catal.*, 2020, **10**, 4906–4913.
247 H. Li, H. Shang, X. Cao, Z. Yang, Z. Ai and L. Zhang, *Environ. Sci. Technol.*, 2018, **52**, 8659–8665.
248 A. L. Teel, S. A. Khotz and R. J. Watts, *J. Adv. Oxid. Technol.*, 2007, **10**, 282–286.
249 R. J. Watts and A. L. Teel, *Water Res.*, 2019, **159**, 46–54.
250 M. Ahmad, M. A. Simon, A. Sherrin, M. E. Tuccillo, J. L. Ullman, A. L. Teel and R. J. Watts, *Chemosphere*, 2011, **84**, 855–862.
251 C. Zhang, T. Li, J. Zhang, S. Yan and C. Qin, *Appl. Catal., B*, 2019, **259**, 118030.
252 Q. Wang, H. Zhou, X. Liu, T. Li, C. Jiang, W. Song and W. Chen, *Environ. Sci.: Nano*, 2018, **5**, 2864–2875.
253 R. J. Watts, B. C. Bottenberg, T. F. Hess, M. D. Jensen and A. L. Teel, *Environ. Sci. Technol.*, 1999, **33**, 3432–3437.
254 J. Xiao, Y. Xie, Q. Han, H. Cao, Y. Wang, F. Nawaz and F. Duan, *J. Hazard. Mater.*, 2016, **304**, 126–133.
255 J. Jiang, Z. Lu, M. Zhang, J. Duan, W. Zhang, Y. Pan and J. Bai, *J. Am. Chem. Soc.*, 2018, **140**, 17825–17829.
256 A. Ishak, K. Dayana, M. H. Mamat, M. F. Malek and M. Rusop, *Optik*, 2015, **126**, 1610–1612.
257 Z. Li, W. Yang, L. Xie, Y. Li, Y. Liu, Y. Sun, Y. Bu, X. Mi, S. Zhan and W. Hu, *Appl. Surf. Sci.*, 2021, **549**, 149262.

 

258 Z. Wang, H. Jia, T. Zheng, Y. Dai, C. Zhang, X. Guo, T. Wang and L. Zhu, *Appl. Catal., B*, 2020, **272**, 119030.
259 Y. H. Kim and B. C. Chung, *J. Org. Chem.*, 1983, **48**, 1562–1564.
260 X. Xiao, J. Jiang and L. Zhang, *Appl. Catal., B*, 2013, **142**, 487–493.
261 A. Yuan, H. Lei, Z. Wang and X. Dong, *J. Colloid Interface Sci.*, 2020, **560**, 40–49.
262 S. Ito, Y. Kon, T. Nakashima, D. Hong, H. Konno, D. Ino and K. Sato, *Molecules*, 2019, **24**, 2520.
263 F. Xie, Y. Zhang, X. He, H. Li, X. Qiu, W. Zhou, S. Huo and Z. Tang, *J. Mater. Chem. A*, 2018, **6**, 13236–13243.
264 C. Chen, G. Qiu, T. Wang, Z. Zheng, M. Huang and B. Li, *J. Colloid Interface Sci.*, 2021, **592**, 1–12.
265 V. R. Akhmetova, G. R. Khabibullina, E. B. Rakhimova, R. A. Vagapov, R. R. Khairullina, Z. T. Niatshina and N. N. Murzakova, *Mol. Diversity*, 2010, **14**, 463–471.
266 S. Kobayashi, Y. Mori, J. S. Fossey and M. M. Salter, *Chem. Rev.*, 2011, **111**, 2626–2704.
267 J. H. Xie, S. F. Zhu and Q. L. Zhou, *Chem. Rev.*, 2011, **111**, 1713–1760.
268 Q. Li, X. Huang, G. Su, M. Zheng, C. Huang, M. Wang, C. Ma and D. Wei, *Environ. Sci. Technol.*, 2018, **52**, 13351–13360.
269 A. Khampuanbut, S. Santalelat, A. Pankiew, D. Channei, S. Pornsuwan, K. Faungnawakij, S. Phanichphant and B. Inceesungvorn, *J. Colloid Interface Sci.*, 2020, **560**, 213–224.
270 J. L. Shi, H. Hao and X. Lang, *Sustainable Energy Fuels*, 2019, **3**, 488–498.
271 E. J. Corey and W. C. Taylor, *J. Am. Chem. Soc.*, 1964, **86**, 3881–3882.
272 C. S. Foote and S. Wexler, *J. Am. Chem. Soc.*, 1964, **86**, 3880–3881.
273 T. Li, L. Ge, X. Peng, W. Wang and W. Zhang, *Water Res.*, 2021, **190**, 116777.
274 L. He, Z. W. Jiang, W. Li, C. M. Li, C. Z. Huang and Y. F. Li, *ACS Appl. Mater. Interfaces*, 2018, **10**, 28868–28876.
275 R. Luo, M. Li, C. Wang, M. Zhang, M. A. Nasir Khan, X. Sun, J. Shen, W. Han, L. Wang and J. Li, *Water Res.*, 2019, **148**, 416–424.
276 S. Liu, Z. Zhang, F. Huang, Y. Liu, L. Feng, J. Jiang, L. Zhang, F. Qi and C. Liu, *Appl. Catal., B*, 2021, **286**, 119921.
277 F. Sun, T. Chen, H. Liu, X. Zou, P. Zhai, Z. Chu, D. Shu, H. Wang and D. Chen, *Sci. Total Environ.*, 2021, **784**, 147117.
278 J. Zhao, F. Li, H. Wei, H. Ai, L. Gu, J. Chen, L. Zhang, M. Chi and J. Zhai, *Chem. Eng. J.*, 2021, **409**, 128150.
279 J. Li, J. Miao, X. Duan, J. Dai, Q. Liu, S. Wang, W. Zhou and Z. Shao, *Adv. Funct. Mater.*, 2018, **28**, 1804654.
280 Y. X. Chen, J. Y. Gao, Z. W. Huang, M. J. Zhou, J. X. Chen, C. Li, Z. Ma, J. M. Chen and X. F. Tang, *Environ. Sci. Technol.*, 2017, **51**, 7084–7090.
281 J. Lee, S. Hong, Y. Mackeyev, C. Lee, E. Chung, L. J. Wilson, J. H. Kim and P. J. J. Alvarez, *Environ. Sci. Technol.*, 2011, **45**, 10598–10604.
282 A. Kashyap, E. Ramasamy, V. Ramalingam and M. Pattabiraman, *Molecules*, 2021, **26**, 2673.
283 Z.-J. Li, S. Li, A. H. Davis, E. Hofman, G. Leem and W. Zheng, *Nano Res.*, 2020, **13**, 1668–1676.
284 P. K. Dikshit, S. K. Padhi and V. S. Moholkar, *Bioresour. Technol.*, 2017, **244**, 362–370.
285 S. Zhao, Z. Dai, W. Guo, F. Chen, Y. Liu and R. Chen, *Appl. Catal., B*, 2019, **244**, 206–214.
286 H. Li, X. Li, J. Zhou, W. Sheng and X. Lang, *Chin. Chem. Lett.*, 2021, DOI: **10.1016/j.cclet.2021.10.068**.
287 S. Xu, P. Zhou, Z. Zhang, C. Yang, B. Zhang, K. Deng, S. Bottle and H. Zhu, *J. Am. Chem. Soc.*, 2017, **139**, 14775–14782.
288 N. Zheng, X. He, R. Hu, R. Wang, Q. Zhou, Y. Lian and Z. Hu, *Appl. Catal., B*, 2022, **307**, 121157.
289 M. Sajid, X. Zhao and D. Liu, *Green Chem.*, 2018, **20**, 5427–5453.
290 C. He, J. Cheng, X. Zhang, M. Douthwaite, S. Pattisson and Z. Hao, *Chem. Rev.*, 2019, **119**, 4471–4568.
291 Y. Li, C. Wang, C. Zhang and H. He, *Top. Catal.*, 2020, **63**, 810–816.
292 P. Pinto Joseph, G. R. Gladstone and L. Yung Yuk, *Science*, 1980, **210**, 183–185.
293 C. Dong, Z. Qu, Y. Qin, Q. Fu, H. Sun and X. Duan, *ACS Catal.*, 2019, **9**, 6698–6710.
294 Y. Ma, L. Wang, J. Ma, H. Wang, C. Zhang, H. Deng and H. He, *ACS Catal.*, 2021, **11**, 6614–6625.
295 Z. Wang, W. Wang, L. Zhang and D. Jiang, *Catal. Sci. Technol.*, 2016, **6**, 3845–3853.
296 M. He, J. Ji, B. Liu and H. Huang, *Appl. Surf. Sci.*, 2019, **473**, 934–942.
297 X. Liu, J. Mi, L. Shi, H. Liu, J. Liu, Y. Ding, J. Shi, M. He, Z. Wang, S. Xiong, Q. Zhang, Y. Liu, Z. S. Wu, J. Chen and J. Li, *Angew. Chem., Int. Ed.*, 2021, **60**, 26747–26754.
298 T. Brink Gerd Jan, W. C. E. Arends Isabel and A. Sheldon Roger, *Science*, 2000, **287**, 1636–1639.
299 F. Sabaté, J. L. Jordá, M. J. Sabater and A. Corma, *J. Mater. Chem. A*, 2020, **8**, 3771–3784.
300 Y. Dong, J. Luo, S. Li and C. Liang, *Catal. Commun.*, 2020, **133**, 105843.
301 Y. Dai, P. Ren, Y. Li, D. Lv, Y. Shen, Y. Li, H. Niemantsverdriet, F. Besenbacher, H. Xiang and W. Hao, *Angew. Chem., Int. Ed.*, 2019, **131**, 6331–6336.
302 E. Markó István, R. Giles Paul, M. Tsukazaki, M. Brown Stephen and J. Urch Chistopher, *Science*, 1996, **274**, 2044–2046.
303 I. Enache Dan, K. Edwards Jennifer, P. Landon, B. Solsona-Espriu, F. Carley Albert, A. Herzing Andrew, M. Watanabe, J. Kiely Christopher, W. Knight David and J. Hutchings Graham, *Science*, 2006, **311**, 362–365.
304 M. J. Schultz, R. S. Adler, W. Zierkiewicz, T. Privalov and M. S. Sigman, *J. Am. Chem. Soc.*, 2005, **127**, 8499–8507.
305 H. Yan, Q. Shen, Y. Sun, S. Zhao, R. Lu, M. Gong, Y. Liu, X. Zhou, X. Jin, X. Feng, X. Chen, D. Chen and C. Yang, *ACS Catal.*, 2021, **11**, 6371–6383.
306 Y. Wan and J. M. Lee, *ACS Catal.*, 2021, **11**, 2524–2560.

307 E. Hayashi, T. Komanoya, K. Kamata and M. Hara, *ChemSusChem*, 2017, **10**, 654–658.
308 X. Han, C. Li, X. Liu, Q. Xia and Y. Wang, *Green Chem.*, 2017, **19**, 996–1004.
309 S. Zhang, X. Sun, Z. Zheng and L. Zhang, *Catal. Commun.*, 2018, **113**, 19–22.
310 X. Wan, N. Tang, Q. Xie, S. Zhao, C. Zhou, Y. Dai and Y. Yang, *Catal. Sci. Technol.*, 2021, **11**, 1497–1509.
311 F. Sabaté, J. L. Jordà and M. J. Sabater, *Catal. Today*, 2021, DOI: **10.1016/j.cattod.2021.06.033**.
312 S. Ishikawa, Y. Yamada, C. Qiu, Y. Kawahara, N. Hiyoshi, A. Yoshida and W. Ueda, *Chem. Mater.*, 2019, **31**, 1408–1417.
313 L. Bui, R. Chakrabarti and A. Bhan, *ACS Catal.*, 2016, **6**, 6567–6580.
314 T. Li, F. Liu, Y. Tang, L. Li, S. Miao, Y. Su, J. Zhang, J. Huang, H. Sun, M. Haruta, A. Wang, B. Qiao, J. Li and T. Zhang, *Angew. Chem., Int. Ed.*, 2018, **57**, 7795–7799.
315 J. S. Chung, R. Miranda and C. O. Bennett, *J. Catal.*, 1988, **114**, 398–410.
316 S. P. Bates, M. J. Gillan and G. Kresse, *J. Phys. Chem. B*, 1998, **102**, 2017–2026.